UCLA
UCLA Electronic Theses and Dissertations

Title

Advancing Quantitative Perfusion Abdominal Imaging

Permalink

https://escholarship.org/uc/item/4ts326dg

Author

Martin, Thomas Boyd

Publication Date

2018

Supplemental Material

https://escholarship.org/uc/item/4ts326dg#supplemental

Peer reviewed|Thesis/dissertation

UNIVERSITY OF CALIFORNIA

Los Angeles

Advancing Quantitative Perfusion Abdominal Imaging

A dissertation submitted in partial satisfaction of the

requirements for the degree Doctor of Philosophy

in Biomedical Physics

by

Thomas Boyd Martin

2018

ABSTRACT OF THE DISSERTATION

Advancing Quantitative Perfusion Abdominal Imaging

By

Thomas Boyd Martin

Doctor of Philosophy in Biomedical Physics

University of California, Los Angeles, 2018

Professor Kyunghyun Sung, Chair

Purpose

To develop and investigate a self-gated MR imaging technique to improve motion compensation robustness for dynamic contrast enhanced MRI, to develop and evaluate a low-dose CT perfusion reconstruction technique, and to develop motion tracking for uterine motion and evaluate its characteristics in MRI. These all could potentially allow for more practical applications of quantitative MRI and CT in clinical workflow.

Methods

A 3D dual-echo golden angle stack-of-radial gradient echo sequence was developed such that a fat-only self-gated signal (SGS_F) could be extracted using a two-point Dixon method.

The SGS$_F$ was validated by i) numerical simulations of SGS$_F$ in the presence of B$_0$ inhomogeneities and varying fat fractions, ii) comparing to conventional SGS and an external video for respiratory motion detection, and iii) comparing SGS's in four liver DCE MRI scans.

A previously developed MRI reconstruction technique called k-space weighted image contrast (KWIC) was used to reduce the number of x-ray projections per gantry rotation, therefore reducing the radiation dose for CT perfusion (CTP) imaging. KWIC reconstruction was evaluated on i) a numerically simulated FORBILD head phantom with numerically simulated time-varying objects using multiple projection undersampling amounts (50%, 25%, and 12.5% of the original dose) and compared to conventional CT reconstruction, and ii) three clinical CTP cases. Quantitative perfusion metrics were computed and compared between KWIC reconstructed CTP data and those of standard FBP reconstruction.

The 3D golden angle stack-of-radial gradient echo sequence and KWIC reconstruction were then used to scan sixty-one pregnant women. Forty-eight subjects were scanned between 14-18 weeks and 19-24 weeks gestational age (GA). Thirteen additional pregnant subjects underwent only a single MRI between 14-18 weeks GA. An image-based algorithm was used on 3D dynamic images to track uterine motion over time in the superior-inferior and left-right directions. Uterine contraction and maternal motion cases were separated and compared between GA, fetal sex, and placental location. Comparisons were done in relation to direction and duration of the uterine motion. An unpaired t-test and a paired t-test were performed between GA, fetal sex, and placental location in terms of direction and duration for uterine contraction and maternal related motion, respectively.

Results

Numerical simulation showed that the fat extraction for SGS has less than 15% error at $\Delta f = \pm 0\text{-}50$ Hz. There is strong correlation between SGS and SGS_F (mean correlation = 0.91), and video motion curve and SGS_F (mean correlation coefficient = 0.87). $SGS_F(t)$ was not significantly affected by the contrast uptake in liver DCE MRI experiment.

For the CT perfusion the numerical simulations showed that KWIC were unaffected by the undersampling/dose reduction (down to 12.5% dose) with KWIC reconstruction compared to the fully sampled FBP reconstruction. The normalized root-mean-square-error (NRMSE) of the AUC in the FORBILD head phantom is 0.04, 0.05 and 0.07 for 50%, 25%, and 12.5% KWIC respectively as compared to FBP reconstruction. The cerebral blood flow (CBF) and cerebral blood volume had no significant difference between FBP and 50%, 25%, and 12.5% KWIC reconstructions (p>0.05).

In uterine motion we observed the mean duration of the contractions was significantly longer by 26.5 seconds during GA 14-18 weeks compared to GA 19-24 weeks (p=0.034) and significantly longer for male fetuses versus female fetuses (p=0.044; 141.7 ± 20.1s and 106.9 ± 43.2s, respectively). There was no significant difference between duration and direction in maternal-related motion by GA, fetal sex, or placental location (p > 0.05).

Conclusions

Respiratory motion correction in the liver can be achieved using fat-only SGS with minimal error in the fat-water separation. The proposed technique has potential implications for more robust motion correction for liver dynamic contrast enhanced MRI.

The low dose CTP study demonstrates that KWIC preserves perfusion metrics for CTP with substantially reduced dose. Clinical implementation will require further investigation into methods of rapid switching of a CT X-ray source.

There is a significant difference in the duration of uterine contractions between the two gestational ages examined and the fetal sex. No association in maternal motion during early gestation was seen between GA, fetus sex and placental position.

The dissertation of Thomas Boyd Martin is approved.

Danny Jiong Jiong Wang

Michael McNitt-Gray

Holden H Wu

Peng Hu

Kyunghyun Sung, Committee Chair

University of California, Los Angeles

2018

This is dedicated to

My dear wife Kelsie, and to my two angels Ammon and Lily

TABLE OF CONTENTS

LIST OF TABLES

LIST OF FIGURES

LIST OF EQUATIONS

ACKNOWLEDGEMENTS

I would like to express my sincere gratitude to my advisor, Dr Kyunghyun Sung. He welcomed me into his lab after me needing to switch labs, and he also helped the transition go as smoothly as possible. He has been a great support during good and hard times during my research. He has helped to really understand how to not just do research, but also how to communicate it clearly to everyone. It has been a true honor working with him. Thank you for all of your help.

I would also like to thank Dr. Danny Wang who was my first advisor before he moved from UCLA to USC. He really got me started in my research and we have had great adventures. He has taught me how to take a promising research project and working hard to go beyond just an academic idea. Even after he moved to USC he has been a continual support in my research. I would also like to give a big thanks to Dr. Peng Hu and Dr. Holden who have helped me through my dissertation process and being apart of my committee.

I want to give a special thanks to Dr. Michael McNitt-Gray, who is also on my dissertation committee. It has been a great honor to know and work with him. Thank you for being such a great to support to me throughout my PhD years, and to give me an opportunity to be apart of the wonderful program. I also want to thank Reth Im, who has helped me make sure that I am on the right path and not forgotten. She took care of all the behind scenes for all the major steps throughout my time hear at UCLA. Even though she is not with us now, I want to thank the late Terry Moore, who was a huge support and really made me feel at home here in the Biomedical Physics program. You are missed.

Thank you Angelia and Jesse for your friendship and kindness throughout my time here at UCLA. They have been great friends and it has been great to have someone to talk to who is also in the program and helping me get through the difficult times that come with a PhD. Thank you to all of my fellow lab mates Xinran, Sam, Alibek, Le, Dapeng, Ziwu, Tess, Andres, Xinzhou for helping me with my projects. They gave support when I was down, and thank you for volunteering for my many MRI scans.

Thank you to my mom and dad who have always been there for me. They have been a solid foundation for me and have provided the means for me to be here where I am today. Thank you for teaching me the importance of gaining an education and being the best person I can be. Thank you to my sisters and brother who have come and visited me and always made feel important.

Lastly and most importantly I wanted to thank my dearest wife Kelsie Martin. She has been with me through the whole time. She has given me loving support and allowed me to spend all this time dedicated to my research. She has worked, given birth to our two kids, stayed at home, and done so much more. I really could not have come this far without her. Thank you Kelsie for all your love and believing in me when I did not believe in myself. Love you with all my heart.

EDUCATION

| 2012 – 2015 | **University of California, Los Angeles** | **Los Angeles, CA** |

M.S., Biomedical Physics

| 2006 – 2012 | **Utah State University** | **Logan, UT** |

B.S., Physics, minor in Mathematics

HONORS & AWARDS

2017   Biomedical Physics Graduate Program Award

2015-2017   Proceedings ISMRM Scientific Sessions Student Stipend Award

First Author Peer Reviewed Publications

1. **Martin T**., Hoffman J., Alger J., McNitt-Gray M., Wang D., Low dose CT Perfusion with projection view sharing. Med. Phys. 2018 Jan. Doi:10.1002/mp.12640.

2. **Martin T**., Wang Y., Rashid S., Shao X., Moeller S., Peng H., Sung K., Wang D., Highly accelerated SSFP imaging with controlled aliasing in parallel imaging and integrated-SSFP (CAIPI-iSSFP). iMRI, 2017 Dec; 21 (4).

3. **Martin T**., Armstrong T., Danyalov A., Lee E., Felker E. Sayre J., Raman S., Wu H., Sung K., Evaluation of fat-only SGS (SGSF) for respiratory motion extraction and compensation in the liver. (Submitted to MRM - Under Revisions)

4. **Martin T.**, Liu D., Li X., Del Rosario I., Chanlaw T., Choi S., Devaskar S., Janzen C., Armstrong T., Masamed R., Wu H., Sung K., MRI characterization of uterine motion in early gestation using image-based motion tracking. (Submitted to JMRI)

Co-Author Peer Reviewed Publications

6. Armstrong T., Wong C., **Martin T.**, Chanlaw T., Devaskar S., Janzen C., Masamed R., Sung K., Wu H., 3D R2* Mapping of the placenta during early gestation using free-breathing multiecho stack-of-radial MRI at 3T, (Accepted in JRMI – In Early View)

7. Zhong X., **Martin T**., Wu H., Nayak K., Sung K., Prostate DCE-MRI with B1+ Correction using an approximated analytical approach. (Accepted in MRM – In Early View)

8. Shao X., Liu D., **Martin T**., Chanlaw T., Sherin D., Janzen C., Murphy A., Margolis D., Sung K., Wang D., Measuring human placental blood flow with multi-delay 3D GRASE pseudo-continuous arterial spin labeling at 3 Tesla. JMRI, 2017 Nov 14. Doi:10.1002/jmri.25893.

9. Sun K., Xue R., Zhang P., Zuo Z., Chen Z., Wang B., **Martin T**., Wang Y., Chen L., He S., Wang D., Integrated SSFP for function brain mapping at 7T with reduced susceptibility artifact. JMR, 276 (2017) 22 - 30.

10. Wang Y., Shao X., **Martin T**., Moeller S., Yacoub E., Wang D., Phase-cycled simultaneous multislice balanced SSFP imaging with CAIPIRINHA for efficient banding reduction. MRM, 2016 Dec;76(6):1764-1774. doi: 10.1002/mrm.26076.

11. Nielsen K., Williams B., Davis E., Smouth-Day K., **Martin T**., Broutman D., Taylor M., Pautet D., Zhao Y., Siskind D., Mitchell N., Moffat-Griffin T., A study of short-period atmospheric gravity waves observed over Other, Antartica. (Submitted to JGR – Under Revisions)

12. Liu D., Shao X., **Martin T.**, Danyalov A., Miao X., Chanlaw T., Janzen C., Devaskar S., Vangala S., Wang D., Sung K., Longitudinal analysis of human placenta perfusion during early gestation with pseudo-continuous arterial spin labeling MRI, (Submitted to Radiology)

Patents

1. **Martin T.**, Hoffman J., Wang D., Reducing Radiation Dose for Dynamic CT Scans.

   Disclosed: 05/13/2015   Provisional Filing: 06/01/2015 (#62/169,498)

Selected Conference Abstracts

Oral Presentations

1. **T Martin**, T Armstrong, E Felker, J Sayre, S Raman, H Wu, K Sung, "Respiratory Motion Compensation in the Liver using Fat-Only Self Gated Signal", Proceedings ISMRM Twenty-Fifth Scientific Sessions, #1003, April 2017

2. **T Martin**, J Hoffman, M McNitt-Gray, DJ Wang, "Low Dose CT Perfusion using Projection View-Sharing", RSNA, SSQ16-03, December 2015

1 INTRODUCTION

Hepatocellular carcinoma (HCC) is a primary malignant liver tumor and is one of the most aggressive malignant cancers causing more than 500,00 deaths per year worldwide[1]. Because it has such a high malignancy, early detection is even more prevalent. One of the common methods of diagnosis is biopsy of liver tissue. However, liver biopsy is invasive and can potentially spread HCC along the needle track[2]. Dynamic contrast-enhanced (DCE) MRI and CT imaging have started to become more widely used because it can capture multiple phase contrasts of the liver to improve detection of the liver metastases. However, qualitative analysis can lead to inter- and intra-reader variability and does not provide accurate staging of HCC. Quantitative DCE-MRI and CT imaging is promising because it can provide quantitative analysis of the cancer reducing the reader variability and provide more accurate staging of HCC. Quantitative DCE-MRI is limited in the liver primarily due to the respiratory motion of the liver. And even though CT is a much faster acquisition time it is limited in clinical practice due to the relatively high amounts of radiation dose to the patient.

Another disorder in the abdominal region is preeclampsia and intrauterine growth restriction (IUGR), and placenta abruption are obstetrical conditions that account for over 50% of all medically indicated preterm birth in the United States[3–5]. Preterm deliveries due to these disorders contribute to higher rates of infant and maternal morbidity and mortality[6]. Therefore, development of accurate methods to predict or detect in early gestation would be of great importance to enable prevention strategies and improve outcomes. One of the current non-invasive methods for assessing placental function is uterine artery Doppler[4]. However, it has low sensitivities for the detection of placental disorders, particularly during early gestation. Quantitative MRI is a promising technique to improve the detection of preeclampsia, IUGR, and placental abruption; however, due to uterine motion caused by patient, uterine contraction, or other organ motion it is limited. Additionally it is not well understood the extent in which these motion artifacts need to be accounted for in MRI.

The purpose of this dissertation is to develop and evaluate a self-gated MR imaging technique to improve motion compensation robustness for DCE-MRI, to develop and evaluate a low-dose CT perfusion reconstruction technique that could potentially allow for more practical applications of DCE MRI and CT in clinical work flow, and to develop a method to evaluate and characterize uterine motion in early gestation to allow for improved motion compensation. The background and overview of these methods are discussed next.

1.1 Quantitative Liver DCE MRI

Quantitative liver DCE-MRI requires continuous acquisition of the whole liver volume for several minutes with each whole image acquired every 5-10 seconds. However it is sometimes limited due to respiratory motion as the liver moves with respiratory breathing. Self-gated signals (SGS) obtained from a golden angle radial trajectory have been shown to be useful for respiratory motion detection and compensation[7]. The SGS is typically extracted by using the central k-space (DC) data from acquired radial spokes and can provide superior / inferior motion (primary direction of the respiratory motion) of the liver. In liver DCE-MRI, the central k-space data are comprised of both the contrast uptakes as well as the respiratory motion. The separation between these two is non-trivial due to the variation in patients' breathing patterns and contrast uptake during the scan, causing inaccurate respiratory motion detection using SGS. The purpose of the study is to develop a fat-only self-gated signal that can be used to inherently separate contrast uptake curve and the respiratory motion signal allowing for more robust motion compensation compared to standard SGS's.

Chapter 2 describes the methods of using recently developed dual-echo 3D golden angle radial gradient echo (GRE) sequence for fat-only respiratory motion extraction. It is a promising technique for liver dynamic contrast enhancement MRI (DCE-MRI), because it has inherent motion robustness, while providing other advantages, such as water-only images and R_2* mapping. It is also described how the fat-only SGS (SGS_F) was developed and evaluated to overcome the issue of contrast uptake and respiratory motion signal using a simple two-point Dixon method to separate fat and water SGS's to improve the motion correction needed for liver DCE-MRI.

1.2 Quantitative DCE-CT

In DCE-CT current dose reduction methods involve low tube-current modulation and iterative reconstruction. However, due to plastic like image reconstruction and long computational times it limits CT perfusion (CTP) imaging in clinical practice. It is theoretically possible to reduce the number of projections by some sort of pulsing of the X-ray tube, which then would allow for undersampled radial reconstruction similar to MRI dynamic imaging and result in lower dose CTP. It is hypothesized that by undersampling the CT projections the radiation dose can be significantly reduced while maintaining diagnostic viability. Chapter 3 describes the work of developing and evaluating using this method of projection undersampling, to allow for dose reduction up to ~75% by adapting a projection view-sharing technique originally developed for accelerated dynamic MRI – k-space weighted image contrast (KWIC).

1.3 Uterine and Placental MRI Imaging

When imaging motion of the placenta and uterus could be caused due to uterine contractions, maternal respiration, fetal motion, and other organ motion[8,9]. In particular, during uterine contractions the uterus compresses, causing significant motion in the uterus and placenta. It has not been well studied the extent these sources of motion are needed to be accounted and adjusted for in MRI imaging. Dickinson et al. studied uterine contraction activity during gestational ages (GA) of 20 weeks – 40 weeks, using a monitor that recorded electrophysiological signals to provide electrocardiogram (ECG) of the fetus heart rate and electrohysterogram (EHG) for uterine contractions[10]. However, only about 70% of the time was the fetal heart rate accurately measured and the EHG reported 19% false positives for uterine contractions. Using 3D dynamic

MR imaging can potentially provide less false positives of uterine contractions, because there is a visualization of the uterine and possibly fetal activity.

Chapter 4 describes the work in how the developed 3D golden angle radial gradient echo sequence developed in Chapter 2 and the KWIC reconstruction was used to track and characterize uterine motion. It is also described how an image-based template matching algorithm was implemented for tracking uterine motion[11,12], and generating motion time plots of the uterus in the super/inferior (SI) and left/right (LR) directions. The goal of the study is to characterize uterine contraction and maternal motion in terms of direction and duration, and to understand if there are associations with gestational age, fetal sex, and placental position are also investigated for uterine contraction and maternal motion.

2 EVALUATION OF FAT-ONLY SELF GATED SIGNAL FOR RESPIRATORY MOTION EXTRACTION AND COMPENSATION IN THE LIVER

2.1 Introduction

Qualitative dynamic contrast enhanced MRI (DCE-MRI) is a widely used technique that can provide initial diagnosis and staging of tumors[13–15]. It has also been shown to be a promising imaging biomarker for monitoring tumor response to chemotherapy, radiotherapy and embolotherapy for breast, prostate, and other cancers[16–20]. In particular, liver DCE-MRI is important in evaluating hepatocellular carcinoma (HCC), liver metastases, and other chronic liver diseases[21–24]. However, many clinical practices in liver MRI are limited to single contrast phase of hepatic artery and portal vein, and require multiple breath holds during contrast

injection[20]. These images can lead to significant intra- and inter-reader variability in qualitative diagnosis. Furthermore, many patients have difficulties properly and consistently holding their breath for the duration of the scan, compromising diagnostic liver MRI image quality.

Quantitative assessment of DCE-MRI is a promising way to evaluate liver diseases objectively since it can provide physiological perfusion parameters of the liver[21,25]. Quantitative DCE-MRI typically requires continuous acquisition of the whole liver volume for several minutes with each whole liver image acquired at every 5-10 seconds[20]. However, the liver can shift up to 20 mm in the superior/inferior (S/I) direction primarily due to respiratory motion[26], and therefore the motion artifacts can significantly limit the quantitative assessment of liver DCE-MRI.

Studies have shown reduced motion artifacts using golden-angle radial sampling[27–30] due to its inherent insensitivity to motion. Additionally, golden angle ordering of radial projections allows for flexible temporal and spatial resolution of the DCE-MRI images due to nearly uniform k-space sampling with arbitrary number projections[31]. However, motion artifacts remain a significant challenge, vary depending on breathing patterns, and decrease the reproducibility of the quantitative images.

The self-gated signal (SGS) obtained from the golden angle radial acquisition has been shown to be useful for respiratory motion detection and compensation[7,27,30,32–34]. The SGS is typically extracted by using the central k-space (DC) data from acquired radial spokes and can

provide superior / inferior motion (primary direction of the respiratory motion) of the liver [30,33]. In liver DCE-MRI, the central k-space data are comprised of both the contrast uptakes as well as the respiratory motion. The separation between these two is not trivial due to the variation in patients' breathing patterns and contrast uptake during the scan, causing inaccurate respiratory motion detection using SGS. If the SGS respiratory motion detection is inaccurate, it can lead to misregistration or not binning the respiratory data in the correct motion state leaving related respiratory motion artifacts in the reconstructed image.

In this work, we propose a novel method for accurately detecting the respiratory motion using fat-only SGS (SGS$_F$) that can be potentially useful in the presence of contrast uptake[35,36]. The SGS$_F$ can be extracted by two-point Dixon fat-water separation[37] using a dual-echo 3D golden angle stack-of-radial sequence. Fatty tissue typically does not include contrast uptake in DCE-MRI, and therefore, the motion detected by SGS$_F$ inherently separates respiratory motion and the contrast uptake signal, thus improving motion compensation in DCE-MRI. The feasibility of using SGS$_F$ is demonstrated by i) performing numerical simulations of the fat-water separation in the presence of B_0 field inhomogeneities, ii) comparing SGS$_F$ to a conventional SGS and an external video source, iii) using SGS$_F$ for respiratory motion compensation in normal liver at 3T, iv) using the SGS in liver DCE MRI patient scans at 3T.

2.2 Theory

The SGS is generated from the DC component of k-space, which is located such that the gradient amplitude is zero. It is basically the sum of all the image contrast into a single voxel. It can be expressed as:

$$SGS(t, TE) = \sum_X \sum_y \left\{ \left[W(x,y)C(t) + F(x,y)e^{i\alpha} \right] R(t) e^{i2\pi \Delta f(x,y)TE} e^{i\phi_1(x,y)} \, \Delta x \Delta y \right\}$$

Equation 2-1

where W and F are the water and fat signal contained in the voxel, t is time, $C(t)$ is the contrast uptake curve (assuming that it only occurs in non-fatty tissue), α is the phase angle of fat relative to that of water at the echo-time (TE), $R(t)$ is the respiratory motion, Δf is the frequency shift due to B_0 field inhomogeneity, and ϕ_1 is the static phase that may arise from other system errors.

For the dual echo sequence, the two signals are acquired such that at TE_1 the fat and water are out-of-phase (OP) to each other and TE_2 the fat and water are in phase (IP), the SGS for OP and IP can be written as,

$$SGS_{OP}(t) = \sum_X \sum_y \left\{ [W(x,y)C(t) - F(x,y)] R(t) e^{i2\pi \Delta f(x,y)TE_1} e^{i\phi_1(x,y)} \, \Delta x \Delta y \right\}$$

Equation 2-2

$$SGS_{IP}(t) = \sum_X \sum_y \left\{ [W(x,y)C(t) + F(x,y)] R(t) e^{i2\pi \Delta f(x,y)TE_2} e^{i\phi_1(x,y)} \, \Delta x \Delta y \right\}$$

Equation 2-3

Assuming Δf is small ($\sim$0Hz) and negligible, the fat-only and water-only self gated signals (SGS$_{F,true}$ and SGS$_{W,true}$) can be computed by using the two-point Dixon method[37] :

$$SGS_{F,true}(t) = \sum_X \sum_y \{[F(x,y)]R(t)e^{i\phi_1(x,y)} \Delta x \Delta y\}$$

Equation 2-4

$$SGS_{W,true}(t) = \sum_X \sum_y \{[W(x,y)]C(t)R(t)e^{i\phi_1(x,y)} \Delta x \Delta y\}$$

 Equation 2-5

Note that SGS$_F$ is the sum of the signal from fatty tissue within the imaged volume, and therefore, a change in SGS$_F$ may represent a change in the volume of lung and liver in the excited slab, which could be used for detecting physiological motion over time. When 3D stack-of-radial golden angle radial acquisition (golden angle sampling in the k_x-k_y plane and Cartesian sampling in the k_z dimension) is used, all the radial spokes are acquired along k$_z$ for a given rotation angle, and then the same acquisition scheme is repeated for the next rotation angle (see Fig. 2-1a). For improved motion detection[30], a SGS profile of the entire volume can be constructed for each rotation angle by taking the 1D Fourier transform along k_z. Lastly, the final SGS profile for motion detection can be constructed by including the SGS profiles from all coils and can be expressed as SGS(z,c,t), where z is the slice location, c is the coil index and t is time index for each rotation angle, as described in Fig. 2-1.
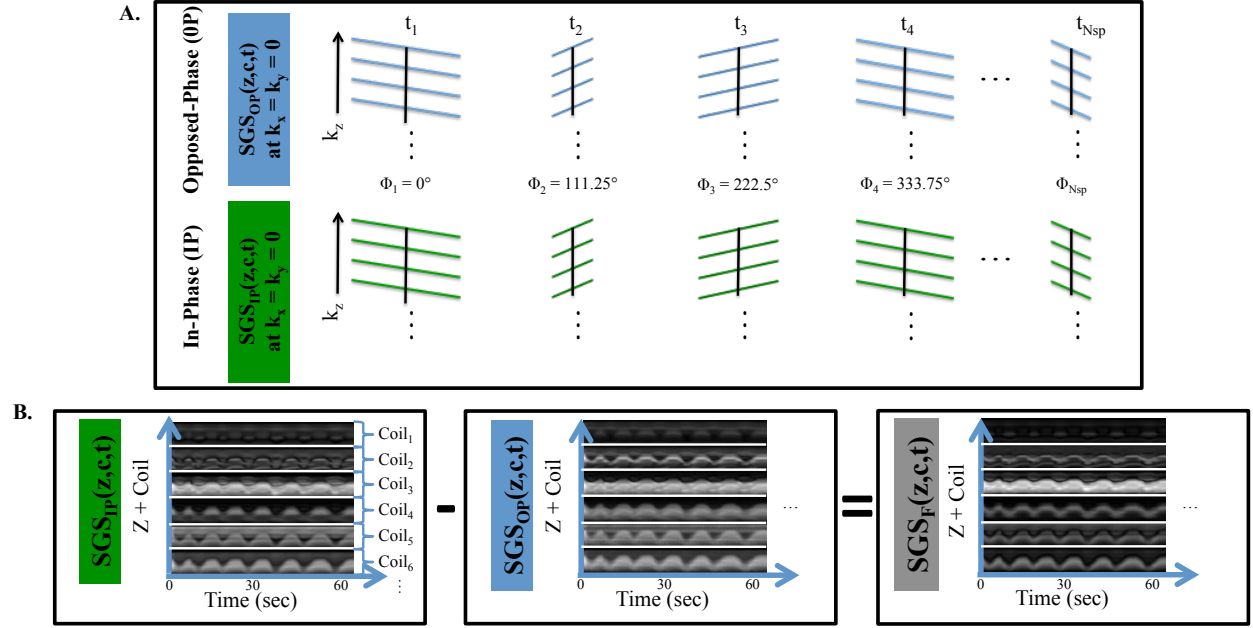
Figure 2-1 A) 3D dual-echo golden angle stack-of-radial acquisition of IP and OP echoes. B) FFT along k_z at $k_x = k_y = 0$ gives $SGS_{IP}(z,c,t)$ and $SGS_{OP}(z,c,t)$. $SGS_F(z,c,t)$ is generated using equation 2-5.

2.3 Methods

2.3.1 Numerical Simulations

When the frequency shift due to B_0 field inhomogeneity, Δf, is not negligible, the fat-water separation using equation 2-4 may not be accurate since SGS_F may include partial contribution from water signal, as expressed below,

$$SGS_F(t) = \frac{1}{2}\sum_X\sum_y\{[W(x,y)C(t) + F(x,y)]e^{i2\pi\Delta f(x,y)TE_2}$$

$$- [W(x,y)C(t) - F(x,y)]e^{i2\pi\Delta f(x,y)TE_1}\}R(t)e^{i\phi_1(x,y)}\,\Delta x\Delta y$$

Equation 2-6

Numerical simulations were performed to evaluate the accuracy of the extracted fat-only SGS using the two-point Dixon fat-water separation. A matrix of 200 x 200 voxels with fat and water

in each voxel was generated. $W(x, y)$ and $F(x, y)$ signals were randomly generated with the mean signal value determined by the desired fat fraction ($FF = \frac{F}{F+W} 100\%$) value between 10-70%. A frequency shift was applied to each voxel in the matrix with linear variation ranging from ±0-50 Hz, to simulate common ranges of frequency shifts at 3T[38–40]. The contrast uptake signal, $C(t)$, was generated by using sample prostate DCE-MRI images to get a general idea of the uptake. The respiratory motion, $R(t)$, was assumed to be a simple sinusoidal curve $R(t) = \sin(wt)$, where w is the respiratory motion frequency and was assumed to be 0.25Hz. Equations 2-2 and 2-3 were then used to generate the SGS$_{IP}$ and SGS$_{OP}$ signals, and SGS$_{F,true}$ was generated using equations 2-4. The mean squared error between SGS$_{F,true}$ and SGS$_F$ (MSE$_{F,F,true}$) was determined as well as the MSE between SGS$_{F,true}$ and SGS$_{W,true}$ (MSE$_{W,F,true}$)

$$MSE_{F,F,true} = \frac{1}{n} \sum_t^n \left(SGS_{F,true}(t) - SGS_F(t) \right)^2$$

Equation 2-7

$$MSE_{W,F,true} = \frac{1}{n} \sum_t^n \left(SGS_{W,true}(t) - SGS_{F,true}(t) \right)^2$$

Equation 2-8

MSE$_{W,F,true}$ represents the maximum possible error that MSE$_{F,F,true}$ can have and a relative percentage error (PE) was calculated as follows:

$$PE(FF, \Delta f) = \frac{MSE_{F,F,true}}{MSE_{W,F,true}} \times 100\% , \begin{cases} FF \in \{0,100\%\} \\ \Delta f \in \{-50,50HZ\} \end{cases}$$

Equation 2-9

2.3.2 Motion Detection

The study was approved by the local Institutional Review Board (IRB), and all subjects provided written informed consent. Thirteen healthy volunteers (age: 26 ± 4 years, weight: 159 ± 34 lbs) were scanned using a 3D dual-echo golden angle radial gradient echo (GRE) sequence on a 3T scanner (Prisma, Siemens Healthcare, Erlangen, Germany) with a 20-channel body matrix array. No contrast media was injected during the scan. The first echo was acquired such that the fat and water signals were out-of-phase (OP; $TE_1 = 1.23$ ms) and the second echo was acquired when the fat and water signals were in-phase (IP; $TE_2 = 2.46$ ms) at 3T. The total scan time was about 3 min, which would include the typical time to acquire pre-contrast, arterial, portal venous, and delayed phases, if there was injection of contrast media. See Table 2-1 for the imaging protocol.

Imaging Parameters	Multi-Echo GA Radial GRE
Number of Echoes	2
TE_1 (ms)	1.23
TE_2 (ms)	2.46
TR (ms)	3.85
Matrix Size	256 x 256 x 48
FOV (mm^3)	380 x 380 x 144
Slice Thickness (mm)	4
Radial Spokes	1000
Bandwidth (kHz)	1370
Flip Angle (degrees)	7
Scan Time (min:sec)	3:04

Table 2-1 Scanning protocol for Dual-Echo GA Radial GRE

The subjects were instructed to perform normal, deep, or a combination of the two (changing half way through the scan) breathing patterns. This was to try to observe different breathing patterns that might be seen in practice. We averaged the two k-space center points to adjust for some gradient delays. We then took the 1D Fourier transform at $k_x = k_y = 0$ along k_z to construct the SGS profiles for IP and OP, $SGS_{IP}(z,c,t)$ and $SGS_{OP}(z,c,t)$ respectively, and $SGS_F(z,c,t)$ was computed using equation 2-5 (see Fig 2-1b). A hamming window filter was applied for temporal filtering and to adjust for high frequency variances in the SGS profiles. For respiratory motion over time, we combined the SGS_F profiles into one-dimensional signal as a function of time, $SGS_F(t)$, which contains the relative respiratory motion. First to combine coil information, we used singular-value decomposition (SVD)[41] to create a single virtual coil that has the dominant signal containing motion information, $SGS_F(z,t)$. Although it is possible to empirically or systematically choose the single coil with the best motion information as each coil contains local respiratory motion information, it is practically very challenging and therefore, it was out of the scope of the study. Lastly, the cross-correlation was performed between a reference projection profile time point and all the projection profiles (see Fig 2-2). The cross-correlation gives a relative position shift between the two-time points. This shift is then used as the final self-gated signal $SGS_F(t)$. In other studies[30,33], the conventional SGS technique is similar to $SGS_{OP}(t)$ because the echo-time desired is short and contains both fat and water signal. Therefore, $SGS_{OP}(t)$ was used as the conventional SGS technique and compared with $SGS_F(t)$ by performing a linear correlation between the two signals.
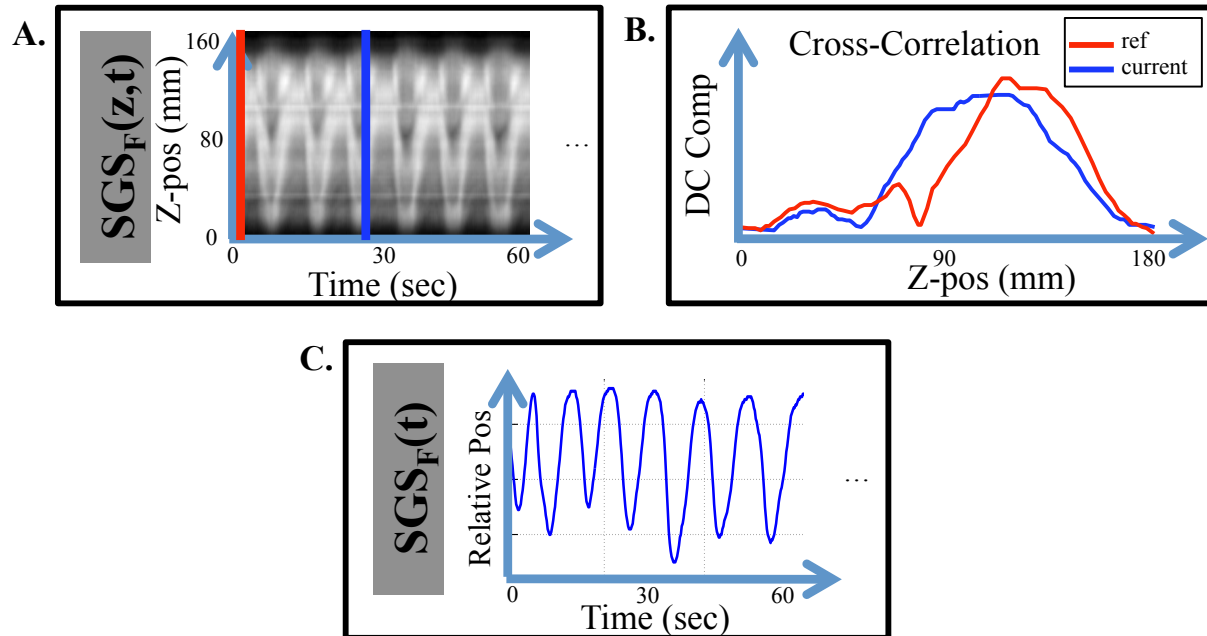
Figure 2-2 Diagram of respiratory motion extraction from SGS$_F$(z,t) ,A), after coil combination. B) Cross-correlation is then used to generate C), the final respiratory motion signal SGS$_F$(t).

2.3.3 External Validation

External videos were recorded for additional validation of motion detection for six subjects (a total of 13 cases). A colored fiducial was placed on subject's chest, and a camera was set up to record their chest motion. To extract respiratory motion, each video frame was first blurred using Gaussian filtering, and a mask of the fiducial was generated by either performing a thresholding or computing an edge of the fiducial mask when the colored fiducial was not sufficiently homogeneous. The center of mass was determined after the mask was generated, and the Euclidian distance between two centers of mass (a reference time point and the other time frame) was computed to generate the video motion curve. The supplementary video shows an example of the external video of a subject breathing with a fiducial and the motion curve extracted from the fiducial. Finally, the video motion curves and SGSs were slightly shifted to account for timing mismatch, and the SGS signals were inverted to match the end inhale motion state. The correlation coefficients were computed to compare the video motion curves to SGS$_F$ and SGS$_{OP}$.

2.3.4 Motion Compensation In-vivo Liver

To show the feasibility of using SGS_F, a static image was reconstructed with and without motion correction for thirteen healthy subjects. Images with no motion correction used all of the spokes acquired during the scan. The motion correction was performed by binning the data into 6 motion states, and then using the motion state with the most radial spokes to reduce the undersampling artifacts. The motion state that had the most radial spokes was at end expiration. For motion corrected reconstructed images, the k-space data from the motion state that had the mode number of radial spokes was used (mean radial spokes ~250, undersampling factor ~1.6). The motion state used was primarily in the end-expiration phase of the respiration. The reconstruction was performed offline (MATLAB; Mathworks, MA; version R2013a) using radial gridding with linear density compensation function.

Two experienced radiologists were given images, with and without motion correction (SGS_F and SGS_{OP}), reformatted in the coronal plane (through plane motion), because this is the main direction of respiratory motion, with no patient information and were blinded to what reconstruction method was used. They scored the images from 1 to 5 based on the motion artifacts (1 = severe motion artifacts, 2 = moderately severe motion artifacts, 3 = moderate motion artifacts, 4 = minimal motion artifacts, and 5 = no detectable motion artifacts). A score of 3 was the minimum score for the image to be a clinically viable image. An intraclass correlation coefficient (ICC) test was used for comparison of inter reader agreement between the

two radiologists. Then a Wilcoxon signed rank test was performed to compare the means with and without motion correction using SGS_F and SGS_{OP}.

2.3.5 Patient Liver DCE MRI

Four patients (age: 64.5 ± 4.5 years, weight: 184 ± 45 lbs) were recruited that were going to have a clinical routine liver DCE MRI study. All patients received gadoxetate disodium (Eovist; Bayer Healthcare, Berlin, Germany) intravenously for their MR imaging examinations with an injection rate of 2.0 mL/sec. A total of 20 ml was intravenously administered, where the contrast agent was diluted 1:1 with saline. The patients were continuously scanned using the 3D golden angle radial GRE sequence to acquire pre-contrast, arterial, venous, and wash-out phases of the liver DCE for 3.5 min. SGS_F was then compared to SGS_{OP} to show the feasibility of SGS_F in the presence of contrast uptake it.

2.4 Results

2.4.1 Numerical Simulation

The numerically simulated MSE percentage errors (PE) between $SGS_{F,true}$ and SGS_F are shown in Fig 2-3. The simulation shows that there is minimal change of the MSE PE as Δf increases (~1-5% change). The PE is most affected by the FF levels of the numerically simulated SGS_F. The typical range of FF in the field of view for healthy subjects is about 30-50% (see dotted white lines in left plot of figure 2-3). The PE ranged from 1-18% in the typical FF range. At FF < 20% the PE error begins to increase near exponentially. The plot on the right shows the cross

section at $\Delta f = 40$ Hz. This plots shows that the PE is much larger at lower FF levels (<30%) and less than 10%.   These numerical simulations show that even though there is contrast uptake the SGS_F will not be significantly affected, assuming the FF is in the range of 30-50%.
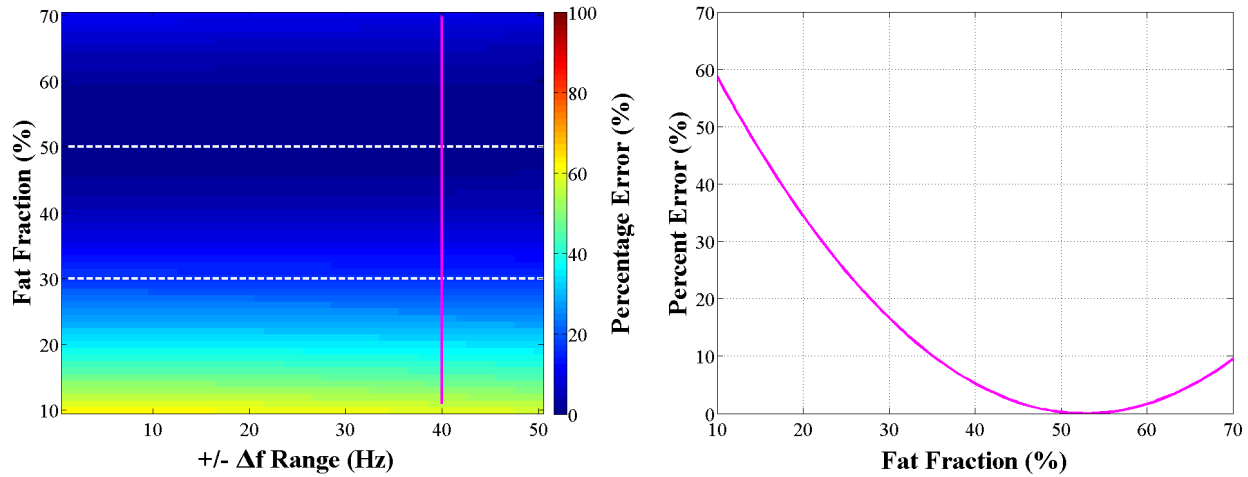
Figure 2-3 The MSE percent error between $SGS_{F,true}$ and the SGS_F (left). The SGS_F is most affected by the FF compared to B_0 inhomogeneities (right plot). The plot on the right shows a cross section of the MSE PE at $\Delta f = 40$Hz. For common FF (30-50%) MSE PE is less than 15% for all fat fraction levels.

2.4.2 Motion Detection

Figure 2-4 (top) shows the $SGS_{OP}(t)$ and the $SGS_F(t)$ plots for one of cases where the patient is performing deep breathing.   The bottom plot is the linear correlation between the two SGS signals.   This example shows a strong positive correlation between $SGS_{OP}(t)$ and $SGS_F(t)$ with a slope of 0.99. The mean slope for all cases was 0.91 ± 0.12.   This shows that there are minimal discrepancies between $SGS_{OP}(t)$ and $SGS_F(t)$ for respiratory motion extraction.
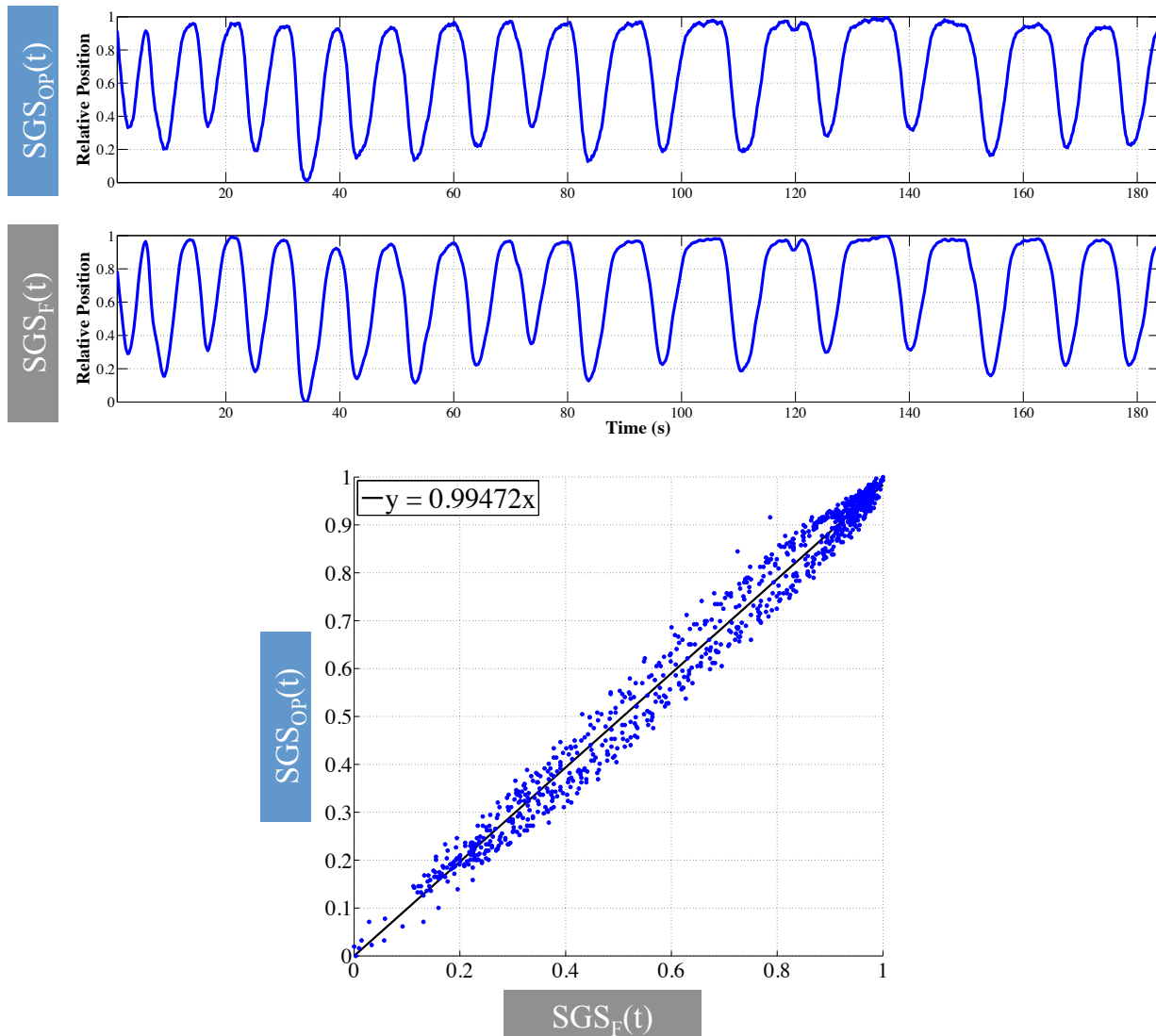
Figure 2-4 SGS$_{OP}$(t) and SGS$_F$(t) comparison with a deep respiration breathing pattern (top). Linear correlation plot comparing the SGS$_{OP}$(t) and SGS$_F$(t) shows a strong positive linear relationship between the two signals. For all thirteen subjects the mean slope is 0.91 ± 0.12.

2.4.3 External Validation

A representative case of the comparison between SGS$_{OP}$(t), SGS$_F$(t), and video motion(t) plots is shown in Fig 2-5. In this case the subject was performing deep breathing, and the peaks and the valleys of the video motion correlate well with the SGS's. The linear correlation coefficient values are 0.87 for SGS$_F$(t) vs. video motion(t) and 0.88 for SGS$_{OP}$(t) vs. video motion(t). A supplementary video is shown how the video motion extraction is performed.
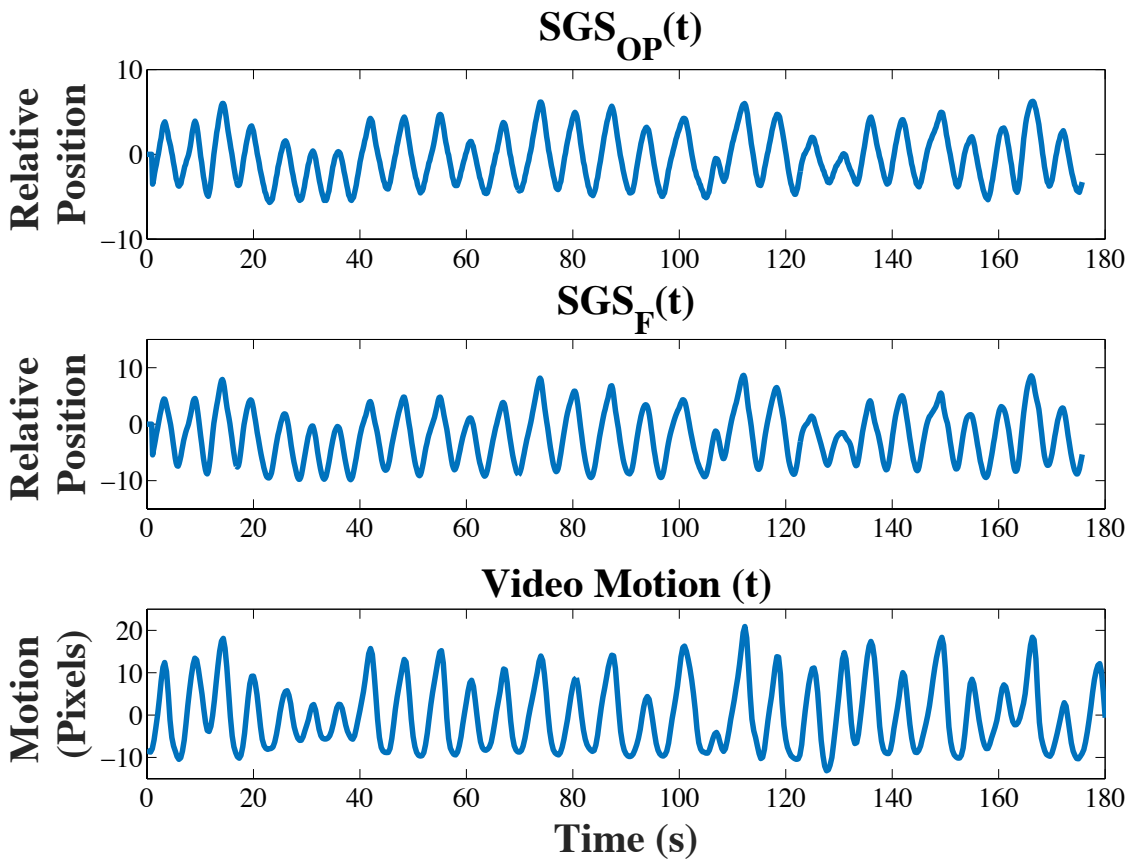
Figure 2-5 A representative plot of the SGS$_{OP}$(t), SGS$_F$(t), and video motion(t) time curves. The amplitudes vary between the SGS's and video motion plots, however the linear correlation coefficient between SGS$_{OP}$(t) and video motion(t) is 0.88 and SGS$_F$(t) and video motion(t) is 0.87.

Table 2-2 gives the linear correlation coefficient of SGS$_F$(t) vs. video motion(t) and SGS$_{OP}$(t) vs. video motion(t) for each of the thirteen cases. The mean correlation coefficient was higher for the SGS$_F$(t) vs. video motion(t) (0.87) compared to the SGS$_{OP}$(t) vs. video motion(t) (0.83), however it was not significantly higher. Subject 2 was a case where the subject performed both normal and deep breathing (changed halfway through scan). The correlation coefficients were lower (0.67 and 0.51) compared to the rest of cases. This is primarily due to SGS$_{OP}$ and SGS$_F$ not representing well the changes of breathing patterns (normal vs. deep). The extracted

video motion had much higher amplitudes during deep breathing compared to the self-gated signals. On the other hand, for case 13, the subject also performed combined breathing patterns, and the correlation coefficients are higher (0.81 and 0.81). However, a coefficient greater than 0.5 still shows significant correlation between the SGS's and the video motion.

Case	SGS_F vs. Video Motion	SGS_{OP} vs. Video Motion
1	0.79	0.71
2	0.67	0.51
3	0.90	0.86
4	0.92	0.89
5	0.90	0.87
6	0.94	0.93
7	0.95	0.92
8	0.87	0.88
9	0.88	0.92
10	0.76	0.73
11	0.92	0.92
12	0.97	0.83
13	0.81	0.81
Mean ± Std	0.87 ± 0.08	0.83 ± 0.11

Table 2-2 Linear Correlation Coefficients between video motion and the respective SGS.

2.4.4 Motion Compensation In-vivo Liver

Images were converted to DICOM for viewing and analyzing in OsiriX (Pixmeo Sarl, Bernex, Switzerland) where images were reformatted from axial to coronal. Reconstructed images with and without motion correction of a subject performing deep breathing are shown in Fig 2-6. In the through plane (top row) image without motion correction there is severe blurring at the diaphragm (white arrow) and the blood vessels. The primary direction of motion is in the S/I direction. In the motion corrected image with SGS_F and SGS_{OP} the diaphragm and blood vessels are sharper (white arrows). There are more visible blood vessels in the images with motion correction compared to without motion correction. The in-plane resolution images (bottom row) show that there is improvement in the respiratory motion blurring when using motion correction with SGS_F. The blood vessels are better delineated (white arrows) with motion correction compared to no motion correction. The radiologist score improved from a 2 (no motion correction) to a 5 (both SGS_F and SGS_{OP} motion correction) with no detectable motion-related artifacts.

No Motion Correction   **Motion Correction with SGS_F**   **Motion Correction with SGS_{OP}**
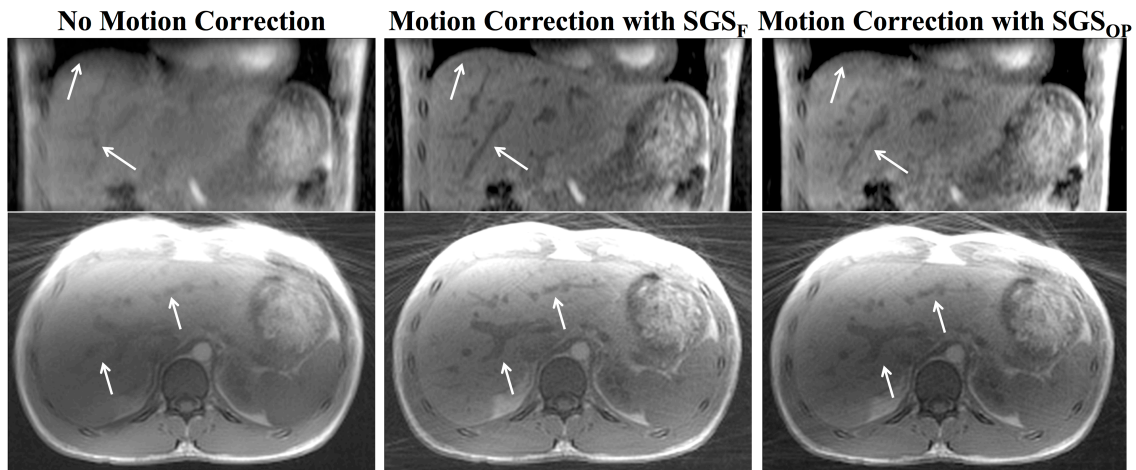
Figure 2-6 Example reconstructed images with SGS_F and SGS_{OP} motion correction and without motion correction. The arrows identify areas of high motion artifacts (left), while after motion correction the motion blurring is greatly reduced (right). The reconstructed images using SGS_F and SGS_{OP} show comparable image quality.

Table 2-3 contains the mean radiologist scores for the reconstructed images with and without motion correction. The ICC comparison showed that there was great statistical inter

reader agreement. Therefore, the radiologist's scores could be combined. The mean radiologist scores were 2.88 ± 1.03, 3.96 ± 0.66, and 3.53 ± 1.10 for images without and with SGS_F and SGS_{OP} motion correction, respectively. The Wilcoxon Signed Rank Tests, comparing the means between each reconstruction method, were all p<0.02, stating that there is a statistically significant difference between all the mean scores, with SGS_F having the highest score. All of the scores of the motion corrected images using SGS_F were 3 and above which corresponds to clinically diagnostic images.

	Radiologist 1	Radiologist 2	Total Mean ± Stdev
No Motion Correction	$3.00 \pm 1.00^{*}$	$2.77 \pm 1.09^{*}$	$2.88 \pm 1.03^{**}$
Motion Correction with SGS$_F$	$4.08 \pm 0.64^{\dagger}$	$3.85 \pm 0.69^{\dagger}$	$3.96 \pm 0.66^{**}$
Motion Correction with SGS$_{OP}$	$3.69 \pm 0.69^{\ddagger}$	$3.38 \pm 0.76^{\ddagger}$	$3.53 \pm 1.10^{**}$

*ICC= 0.94 Intraclass Correlation Coefficient between radiologist scoring
†ICC = 0.86 Intraclass Correlation Coefficient between radiologist scoring
‡ICC = 0.90 Intraclass Correlation Coefficient between radiologist scoring
**p < 0.02 Wilcoxon Signed Rank Test to compare mean scores between each set of images

Table 2-3 Radiologist scoring for no motion correction and motion correction with SGSF images.

2.4.5 Patient Liver DCE MRI

The feasibility of using $SGS_F(t)$ in the presence of contrast uptake is shown in Figure 2-7. The examples of $SGS_F(t)$ and $SGS_{OP}(t)$ from two subjects show that $SGS_F(t)$ is not contaminated with contrast uptake signal while $SGS_{OP}(t)$ includes both respiratory motion and contrast uptake signal. There is a visible rise in $SGS_{OP}(t)$ starting at 90 seconds, while the contrast uptake is not visible in $SGS_F(t)$. Note that there exists a sharp change at the time of the contrast uptake in

subject 2, due to a transient severe motion during hepatic arterial phase associated with gadoxetate disodium[42]. The post-contrast $SGS_F(t)$ levels off at the same amplitude prior to the contrast uptake, while $SGS_{OP}(t)$ remains higher after the contrast uptake. One of the subjects, not shown, there was not a significant amount of contrast uptake seen in neither $SGS_{OP}(t)$ nor $SGS_F(t)$.
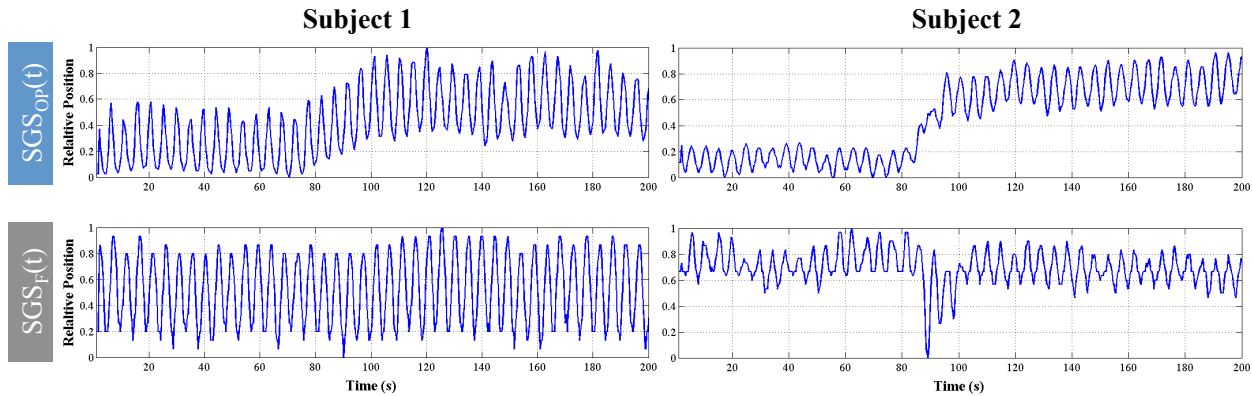
Figure 2-7 Two representative cases of $SGS_{OP}(t)$ and $SGS_F(t)$ in which the subjects underwent liver DCE MRI. Note that subject 2 had a transient severe motion, causing a sharp change in the $SGS_F(t)$ at the time of the contrast uptake (90 seconds).

2.5 Discussion

We have shown that a 3D dual echo golden angle stack-of-radial GRE sequence can be used to properly extract a fat-only SGS, which then can be used for respiratory motion correction on a 3T scanner. The main advantage of extracting a fat-only SGS is that for DCE-MRI scans the SGS will not contain contrast uptake, and eliminate the bias by separating the contrast uptake signal and the respiratory motion signal. The IP and OP echoes can also be used to provide robust water only images compared to using a fat saturation pulse sequence[37,43]. In this study we reconstructed a static image, but golden angle ordering sampling also provides the advantage of having flexible temporal resolution, which can provide the dynamic contrast uptake information needed for quantitative analysis[31].

24

The numerical simulation shows promising results that the MSE PE < 15% at common FF (30-50%). The simulation shows that there is minimal affect (<1% in common FF) of separating out the fat-only SGS in the presence of B_0 inhomogeneity. The numerical simulation included both contrast uptake and respiratory simulations and represents an accurate representation of the SGS with contrast uptake similar to DCE-MRI studies. It is shown that the SGS_F can be appropriately separated in the presence of contrast uptake in water tissue within commone FF levels. It is known that liver fat fraction is often 10% or less, however within the field of view there is also subcutaneous fat and visceral fat. In healthy subjects (not shown in study) fat fraction maps were generated and a mean FF of about 35% was measured within the field of view allowing for minimal error in the fat-water separation in DCE-MRI studies.

It is possible to more accurately separate fat-water in the presence of B_0 inhomogeneities by using methods such as extended two-point Dixon[44,45], three-point Dixon technique with B_0 correction[46] or generalized k-space decomposition with chemical shift correction[47]. The extended two-point Dixon method can be used for phase-correction to reduce B_0 inhomogeneities, but there is less tractability of the fat-water separation. Three-point Dixon and generalized k-space methods correct for B_0 inhomogeneities, but they typically require at least three echoes being acquired which increases the TR and decreases the temporal resolution of the dynamic images. Future studies may include implementing these advanced fat-water methods when higher Δf is expected.

It is possible due to gradient delays that the center of k-space is not accurately acquired and removing the assumption that the gradient amplitude is zero. This would then increase the error in fat-water simulation. However, it has been shown that gradient calibration can be achieved such that the center of k-space is accurately acquired[48].

The SGS_F is comprised of the entire fatty tissue within the imaged volume. This includes subcutaneous fat, liver fat, bone marrow and visceral fat. The PE may be reduced for patients with high amounts of subcutaneous fat or fatty-liver disease (FF = 5%-30%). In this study only healthy and young subjects were included, and have a lower FF in the liver as well as subcutaneous fat compared to most clinical patients.

It was shown that SGS_F was not contaminated with contrast uptake signal for liver DCE-MRI studies. In all four patient cases there was no contrast uptake observed, however in one of the cases there was no contrast uptake observed in either SGS_F or SGS_{OP}. For this case, in the dynamic liver images it was observed that there was a contrast leak prior to the scanning and therefore no contrast uptake in the self-gated signals was observed. It is difficult to quantitatively validate that the contrast uptake signal is separated from the respiratory signal in SGS_F. Future studies could include verifying the contrast uptake separation of SGS_F by using arterial contrast uptake or other tissue and subtract it from SGS_{OP} to get a rough estimation. Another approach is using SGSF for motion compensation and look at the reconstructed images to see if they have reduced motion artifacts.

One of the remaining challenges is a way to find an optimal combination of coils when generating self-gated signal. The coil compression was used for the healthy subjects, but a manual coil selection was performed for liver DCE-MRI to improve self-gated signal. An automated coil selection approach, similar to Zhang et al.[49] would be highly desirable to make it more useful in clinical practice. Further development of the automated coil selection for the SGS in the presence of contrast will be needed in future studies.

For all reconstructed images with motion correction the range of the radiologist scoring was 3 to 5. The minimum score for clinically relevant images was 3, indicating all of the motion corrected images would be clinically viable with minimal motion artifacts. Even with the subjects deep breathing where large motion artifacts were noticed the motion correction improved the radiologist scoring and rendered the previously motion corrupted images more clinically viable. This shows that the SGS_F is accurately representing the liver motion due to respiratory motion. This respiratory information could also be used to perform non-rigid liver motion correction to essentially create a dynamic series of the liver with one motion state[50].

2.6 Conclusion

We have demonstrated that respiratory motion extraction and compensation in the liver can be achieved using fat-only self-navigated signal with minimal error in the fat-water separation (< 15%). The SGS_F is comparable to an external respiratory source (mean linear correlation coefficient = 0.87 ± 0.08) as well as to the conventional SGS (mean linear correlation slope = 0.91 ± 0.12). Images with motion correction using SGS_F all had a radiologist score that were all

clinically relevant and statistically significant, compared to no motion corrected images ($p <$

0.01). It was also shown that the contrast uptake does not significantly affect $SGS_F(t)$. Using this

technique has potential implications for more robust motion correction for liver DCE-MRI due to

its inherent separation between respiratory motion signal and contrast uptake.

3 Low Dose CT Perfusion with Projection View Sharing

3.1 Introduction

CT brain perfusion (CTP) is a widely used imaging technique for the evaluation of hemodynamic changes in stroke and cerebrovascular disorders as well as neoplasm[51]. In acute stroke imaging, CTP of the brain is valuable for the detection of ischemic lesions, and for distinguishing infarct core from penumbra brain tissue in acute stroke[52]. However, CTP involves a high radiation dose for the patients as the CTP scan continuously images the same anatomical region for approximately 60 seconds in order to capture the full passage of the contrast bolus. This has been raised as a concern by the FDA[53], especially when multiple successive CTPs are performed on the same patient, e.g. to monitor reperfusion following recanalization.

Recently, several techniques have been applied for radiation dose reduction in CTP scans, including reduction of tube current and tube voltage, as well as the use of novel noise reduction techniques such as iterative reconstruction (IR)[3,4]. The standard CTP protocols now employ a reduced tube voltage of ~80kV while keeping the tube current below 200mA (typically 150mA), without deterioration of quantitative perfusion values[56]. However, the resultant radiation dose of existing CTP scans (≥~200mGy) is still about 2-3 times higher than that of a standard head CT scan (~60mGy)[57]. More recently, different IR methods for reducing radiation dose without sacrificing image quality have been developed by all major CT manufacturers (e.g. iDose by Phillips Healthcare, ASIR by GE Healthcare, SAFIRE (Sinogram Affirmed Iterative Reconstruction) by Siemens Healthcare, and AIDR by Toshiba Medical Systems)[58]. Although the application of IR in standard CT scans has been improving due to enhanced computational power, its application in CTP is very limited due to the high complexity and computational burden for processing dynamic CTP image series (e.g., Siemens doesn't offer IR options for CTP). A recent study showed that it is feasible to reduce radiation dose of CTP by 50% using the IR algorithm called iDose[51,59,60] developed by Philips, however, the subjective image quality of the resultant CTP with IR is still inferior in about a quarter of the patients[61]. There is a critical and unmet need to develop effective dose reduction techniques for dynamic CTP scans, without sacrificing image quality and speed (i.e., clinical workflow).

In recent years, a number of sparse sampling and reconstruction algorithms have been developed for dynamic MRI with radial trajectories, such as highly constrained back projection (HYPR)[62], k-space weighted image contrast (KWIC)[12], and compressed sensing[30]. Since CT projection data can be converted into "k-space" data according to the central slice theorem, these MRI

algorithms can potentially be adapted for dose reduction of dynamic CT scans such as CTP by acquiring reduced number of projections for each image. As a proof-of-concept, HYPR has been applied for low dose CTP[62–64] that allows for reduced image noise and streaking artifacts from undersampled data sets.

Here we present an alternative strategy to reduce the radiation dose of existing CTP methods by ~75% by adapting a projection view-sharing technique originally developed for accelerated dynamic MRI – k-space weighted image contrast (KWIC) [11,12] We present the theory and provide a proof-of-concept of the proposed technique with numerically simulated phantom data and retrospectively undersampled clinical CTP data. This chapter is based on the published work in Medical Physics[65].

3.2 Theory

As shown in Fig. 3-1a, the standard CT scan involves continuous rotation and exposure of the X-ray source around the patient. According to the Nyquist criterion and standard CT acquisition scheme, a total of $\pi * X_{res}$ (where X_{res} is the number of detectors; π takes into account two projections 180° apart) projection views are acquired to form one CT image. For dynamic CT scans, the total number of X-ray projection views will be $\pi * X_{res} * N_{frame}$ (number of temporal frames, typically 45-60 for CTP), resulting in a high level of radiation dose. As shown in Fig. 3-1b, the proposed technology reduces the radiation dose of CTP scans by controlling the X-ray source to be on intermittently (instead of continuously) at pre-specified rotation angles (e.g., programmed pulsed X-ray). The dynamic CTP image series can then be reconstructed using

algorithms that preserve high spatial and temporal resolutions as well as image quality comparable to those of standard CTP scans.
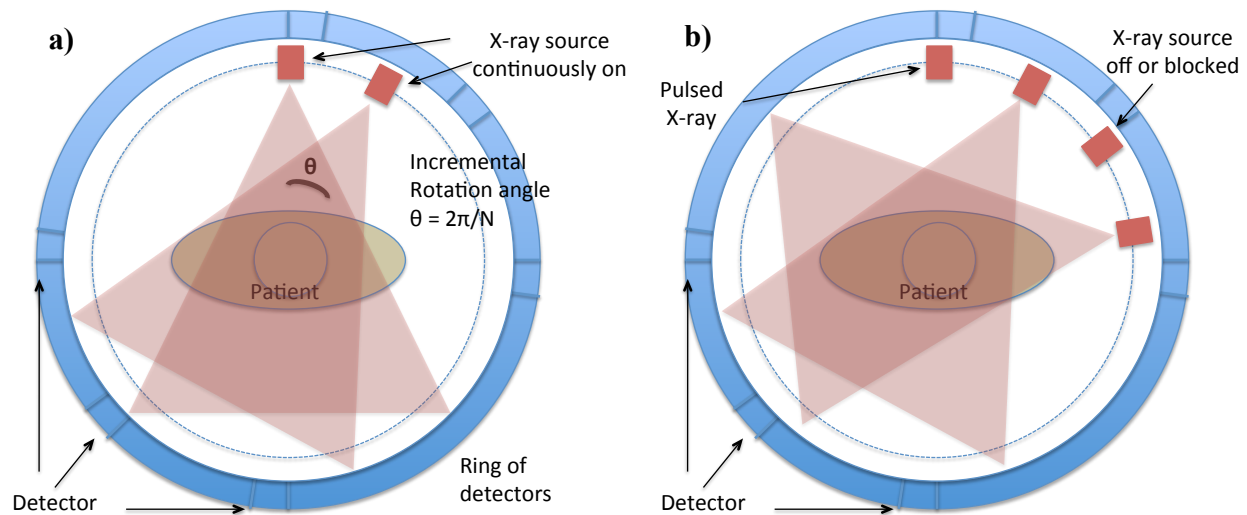
Figure 3-1 a) The standard CT acquisition has the X-ray tube continuously on and acquires projections at 2π/N increments. For KWIC implementation the x-ray tube needs to be intermittently on, b), during gantry rotation at specified angles.

Many algorithms can be applied for this purpose by exploiting the redundancy of information in 4D dynamic imaging data. In this work we focus on a projection view-sharing technique called KWIC which was originally developed for accelerated 4D dynamic MRI with radial trajectories[11,12]. KWIC exploits the oversampling of the k-space center in the radial acquisition by using drastically fewer views in the central region of k-space, while progressively larger numbers of views are used toward the outer k-space regions in a fashion of sub-apertures (Fig. 3-2). The image contrast is primarily determined by the central region of k-space (i.e., low spatial frequencies), therefore relatively few projection views are required to maintain the image contrast with a high temporal resolution. The radius of the central region (ρ_1), and subsequent sub-aperture regions (ρ_n), is based on the Nyquist sampling criteria to minimize undersampled streaking artifacts and is calculated by

$$\rho_n = \frac{N}{\pi(\alpha - n + 1)}$$

Equation 3-1

where *N* is the total number of projections, α is the number of sub-apertures used, and *n* is the

region number (*n* = 1 is central region)[12]. The number of projections in each sub-aperture region

(ρ_n*π) increases progressively with number of sub-apertures toward the outer k-space
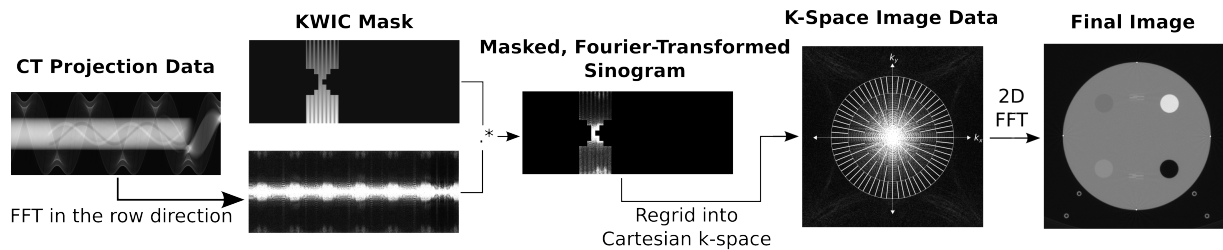
regions[11,12]. A voronoi diagram is then used for density compensation[66].

Figure 3-2 Illustration of the CT-KWIC workflow. Raw CT projection data is Fourier transformed along the detector rows (column direction in this figure depiction) and combined with a KWIC mask, which selects and weights projections into sub-apertures. The masked sinogram is then regridded into 2D Cartesian k-space; a grid is overlaid in this diagram to indicate the relative density of projections in each sub-aperture (fewest at the center "view-core," where contrast info lies, most at the outer, high-frequency regions). The outer sub-apertures will contain the largest amount of view-sharing. Finally, the gridded k-space image will be Fourier transformed into final 2D image.

As a projection view-sharing technique, KWIC is able to preserve high spatial and temporal

resolutions of undersampled 4D dynamic contrast enhanced MRI and MR angiography[27].

Projection imaging data such as CT can be related to the frequency domain (e.g., k-space in

MRI) through the central-slice theorem by performing 1-D FT of the projection of an object,

which is the same as the line drawn through the center of the 2-D FT plane (i.e., k-space). By

converting the CT sinogram into "k-space" data, we can apply KWIC to preserve high spatial

and temporal resolutions of undersampled CTP data by progressively increasing the number of projection views for more distant regions of "k-space" (Fig. 3-2). Under this paradigm, contrast information, most important for quantitative CTP measures such as CBV, CBF, etc., maintains high temporal resolution, and temporal blurring is relegated to high frequency image details that do not impact perfusion measurements.

While the central-slice theorem provides the key connection between CT projection data and k-space used for KWIC reconstructions, parallel-beam CT geometry (e.g. "pencil beam" or translate-rotate geometry[67]) is required for correct mapping. Modern CTP studies are typically conducted using 3rd generation CT scanners with cylindrical detector geometry, which is not immediately suitable for a KWIC reconstruction. To achieve the correct geometry, rebinning algorithms originally developed for helical reconstruction were applied to the projection data, transforming the fan-beam data into "pseudo-parallel" data[68,69]. The rebinning portion of the FreeCT_wFBP reconstruction software was utilized to accomplish this[70].

It should be noted that rebinning involves interpolation and mapping of data from nearby projections in the study. In the case of CTP, this means that the rebinning process itself could result in some amount temporal blurring even prior to the temporal blurring one expects to see from the KWIC algorithm. While this is an important effect to be aware of, it is limited to approximately 0.2 seconds at the edge of the scanner field of view, where it is most severe. Near the center of the scanner field of view, where a head would be placed for a perfusion study, data is interpolated from at most 50-100 nearby projections, or < 0.1 seconds of acquisition data.

This is substantially less than the temporal blurring induced by KWIC and has not been observed to be a source of deviation in perfusion measurements.

Angular rebinning, which induces the temporal blurring, is governed by the equation $\theta=\alpha+\beta$, where θ is the rebinned angle, α is the unrebinned x-ray source angle, and β is the detector channel fan angle[68,69]. Thus, a given projection acquired at angle α, is rebinned into projections of similar source angle, adjusted depending on an individual detector's fan angle. Measurements near the edge of the scanner field of view (i.e. "large" absolute value of β) are rebinned to projections further from its original source angle; measurements near the center of the field (i.e. small β) of view are largely unchanged.

The maximum detector fan angle for the scanner utilized in this is work is 0.436 radians (detectors at the edge of the scanner field of view). 1152 projections are acquired per scanner rotation, which gives an angular increment of 0.00545 rad/projection. Thus, the maximum change in projection index due to rebinning is ±80 projections. With a scanner rotation time of 1 second per rotation, this results in a temporal error of (1/1152)*80=0.07s. Since the blur happens in both the positive and negative directions, all of which will contribute to the reconstruction, we find that at the edge of the field of view, we obtain a temporal blur of 2*0.07=0.14~0.2s due to the angular rebinning. This, however, is still substantially lower than the perfusion sampling rate of 1 sample per second.

The rebinning approach provides benefits as well. Many modern CT scanners employ "flying focal spots" to improve in-plane and z-direction spatial resolution and the rebinning process and software routines used in this work allows for a robust approach to reconstruct scans acquired with flying focal spots using KWIC reconstruction. This requires little to no modification of the KWIC algorithm and allows for improved spatial resolution of the flying focal spot scan. Additionally, once the data is in a parallel geometry, convolution filters can readily be applied to the parallel projection data to modify the spatial and contrast properties of the final reconstruction, as is done in FBP reconstruction; this direct application is not possible in the unmodified diagnostic fan-beam geometry[68]. While not investigated in this work, further dose reduction could be achievable via the careful selection and application of these filters.

3.3 Methods

3.3.1 Adapting K-space weighted image contrast (KWIC) for CTP

A modified KWIC algorithm for reconstruction of CTP data was implemented in MATLAB (The MathWorks Inc., Natick, Massachusetts, USA), that consisted of 5 main modules/steps: 1) rebinning of fan-beam CT data into parallel-beam sinogram data; 2) performing 1D FFT of the projection along the detector row direction; 3) multiplication with a KWIC filter that selects and weights projections into sub-apertures; 4) gridding of KWIC filtered sinogram into 2D Cartesian k-space using the VORONOI algorithm[21]; and finally 5) performing 2D FFT of the regridded k-space data into 2D images (see Fig. 3-2 for diagram of the workflow). Step (1) was implemented using a modified version of freely-available, open-source weighted filtered backprojection (FBP) for CT, FreeCT_wFBP[70].

KWIC divides the k-space into sub-apertures (Fig. 3-3b): the sub-aperture covering the central region of k-space is updated every time frame (or rotation of CT gantry), while progressively larger numbers of views are used in the sub-apertures toward the outer k-space regions and shared between neighboring time frames (Fig. 3-2). The number of projections in the central sub-aperture (or the number of X-ray projections per rotation of CT gantry) is determined by the desired dose reduction. For example, if the standard number of projections is 576 per 180 degrees, and the desired dose reduction is 75%, then the number of projections in the central sub-aperture is 144. The total number of sub-apertures required is also determined by the amount of desired dose reduction as well as the Nyquist sampling criterion in the outer regions of k-space. In this study the minimum number of projections needed in the outmost sub-aperture of k-space is 576 in order to meet the Nyquist criterion. Therefore to achieve 50%, 25%, and 12.5% of the original dose the central sub-aperture would comprise 288, 144, and 72 projections respectively; to satisfy the Nyquist criterion, 2, 4, and 8 sub-apertures are used, respectively.
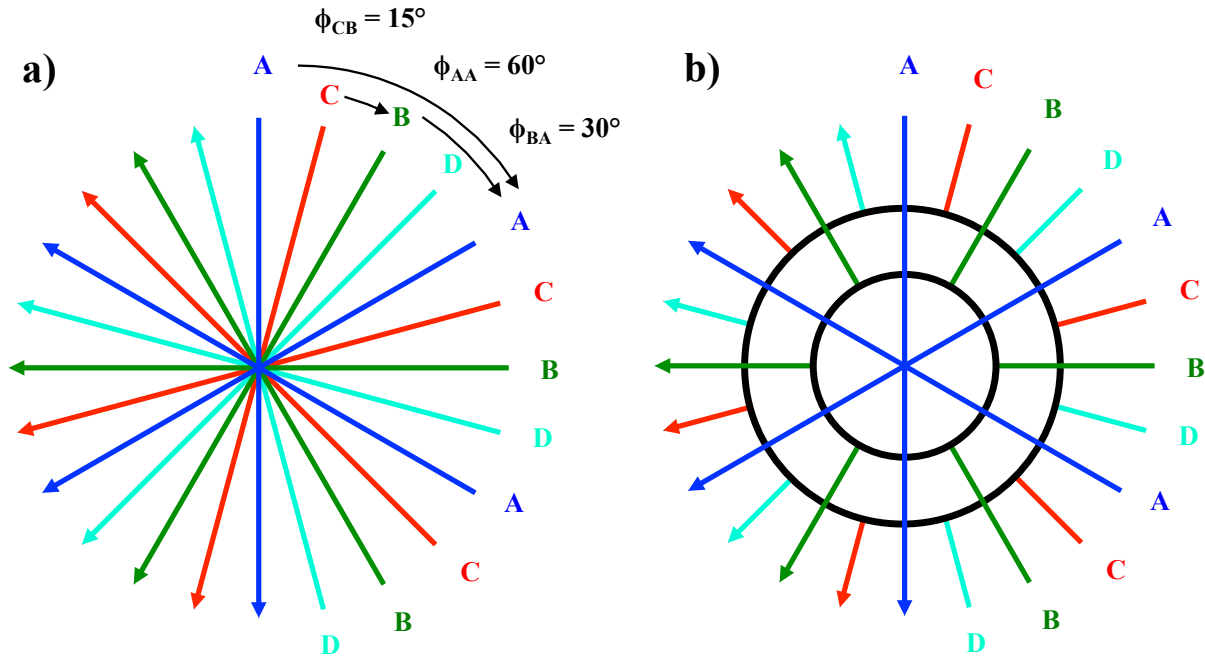
Figure 3-3 Angle-bisection (a) and KWIC reconstruction techniques (b). A, B, C, and D represent sub-apertures that are acquired in an angle-bisection scheme (a). In this example, the time frame projections, A, acquires 3 projections within one gantry rotation with each projection being 60° apart from each other. The next time frame, B, is then acquired such that each projection bisects the angle separation so that the angle between an A and B projection is 30°. C and D sub-apertures are acquired at angles that bisect A to B and B to A projections respectively. The KWIC reconstruction divides the k-space into sub-apertures (b). The sub-aperture in the central region of k-space is updated every time frame (A,B,C,D), while progressively larger numbers of views are used in the sub-apertures toward the outer k-space regions and shared between neighboring time frames.

As mentioned, a clinical implementation of KWIC algorithm also requires a custom acquisition scheme. One potential realization of this is a high speed X-ray switching (e.g. pulsed X-ray) at pre-specified rotation angles to which different sampling sequences of rotation angles can be applied. In the present work, an angle-bisection (or "bit-reverse") sequence of rotation angles for sampling patterns was applied for KWIC. As shown in Fig. 3-3a the projections were acquired in an interleaved fashion (A, B, C, D). During the first gantry rotation, only one downsampled set of evenly distributed projection angles were acquired (A). During subsequent gantry rotations, the projections that bisect the previous set of projections were acquired (B, C, D) until a full set

of projections at all angles were acquired. In other words, one quarter of the projection views are acquired each rotation, corresponding to a 25% dose level per gantry rotation assuming perfect x-ray switching. Data from the different gantry rotations is then assembled by the KWIC reconstruction algorithm into the sub-apertures to achieve complete sampling of k-space. Alternative sampling sequences of rotation angles such as the golden ratio scheme[31,71] may be applied and will be discussed below.

3.3.2 FORBILD Phantom CTP

A FORBILD head phantom containing numerically simulated time-varying objects (5, 10, and 50mm in size) was developed to create a parallel-beam dynamic CT projection data set. The goal was to assess the types of artifacts only the KWIC algorithm will produce. Therefore, the FORBILD head phantom was numerically simulated with no added noise. The time-varying object contrast was simulated using the following gamma-variate equation[72]

$$C(t) = C_0 t^\alpha e^{\alpha(1-t)}$$

Equation 3-2

where C(t) is the contrast signal, C_0 is an arbitrary constant ($C_0 = 1$), t is time, and α is a constant that affects the contrast uptake rise and fall ($\alpha = 11$). The simulated scans were 60 seconds long with 1 gantry rotation per second and 576 projections per 180° rotation. Reduced-dose cases were simulated by down-sampling the number of projections per 180° rotation from 576 to 288 (50% dose), 144 (25%), and 72 (12.5%) based on the angle-bisection scheme. One image per second was reconstructed using FBP and KWIC respectively. KWIC reconstructions utilized 72,

144, and 288 projections per gantry rotation and 4, 3, and 2 sub-apertures, for the 50%, 25% and 12.5% dose cases respectively. On all sets of reconstructed images (FBP 100% dose, KWIC 50% dose, KWIC 25% dose, KWIC 12.5% dose), an ROI was placed on the time-varying object (red ROI dot) and time to peak (TTP), area-under the curve (AUC) and the full width at half maximum (FWHM) of the corresponding dynamic curves were calculated. Perfusion curves produced using the KWIC reconstructions were compared against reference values from the full-dose FBP data.

To assess the effects of the streaking artifacts near the edge of the image, the time-varying object was placed near the back of the FORBILD head phantom. KWIC reconstruction was also performed down to 6.25% of the original dose to show when KWIC reconstruction begins to break down. This was only performed with a 5mm size object, to assess the more extreme case of a lesion in clinical practice. The ROI was drawn on the time-varying object (red ROI dot) and TTP, AUC, and FWHM were measured. To better highlight the artifacts, image subtraction was performed between full dose KWIC reconstruction and the respective low dose KWIC reconstruction. Due to reconstruction algorithm difference, image subtraction was not performed with full dose FBP because it could create spurious artifacts not relevant to the study.

3.3.3 In-vivo CTP data

Three clinical CTP cases were scanned on a Definition AS (Siemens Healthineers, Erlangen, Germany) CT scanner. The scanning parameters are listed in Table 3-1. The CTP protocols used

were the standard clinical protocols for patients with potential strokes, with dose level (217mGy) over 20% lower compared to that of the AAPM recommended protocol (281mGy)[56].

Imaging Parameters	FBP Recon	KWIC Recon
Scan Time (Sec)	45	45
CTDI$_{vol}$ (mGy)	217	N/A
Gantry Rotation (s/turn)	1	1
# Projections/turn	1152	576, 288, 144, 72
Matrix Size	360 x 360	360 x 360
FOV (cm^2)	50 x 50	50 x 50
# Sub-Apertures	1	2,4,8,16
Projections/Sub-Aperture	1152	576, 288, 144, 72
Effective CTDI$_{vol}$ (mGy)	217	109, 55, 28, 14

Table 3-1 Imaging and Reconstruction Parameters

The CTP images were reconstructed using an in-house FBP reconstruction using MATLAB and were compared to KWIC reconstruction at 50%, 25%, and 12.5% dose reduction based on the angle-bisection scheme. Images using all of the projections were also reconstructed using the KWIC algorithm, which is the same as performing gridding reconstruction. For this proof-of-concept study, the central four detector slices of the fan beam data set were averaged together and utilized to achieve an effective slice thickness of 4.8mm, which AAPM recommends as the slice thickness for a Definition AS CT scanner CTP scan protocol[56]. The software used for CTP analysis was SCAN4, which has been used in large-scale clinical trials[73]. Post-processing of CT perfusion images yielded multi-parametric perfusion maps including cerebral blood flow (CBF)

and cerebral blood volume (CBV) by using the delay-insensitive block-circulant singular-value decomposition (bSVD) method according to previously described procedures[74]. Regions-of-interest (ROI) were drawn in the motor cortex for all 3 cases in the CBV and CBF maps to compare between all the reconstructed perfusion maps. A two-tailed t-test was used to compare the mean values of the ROI's for CBF and CBV. The arterial input function (AIF) was extracted from the anterior cerebral artery, venous output function (VOF) from the sagittal sinus vein, and the tissue density signals from manually drawn regions of interest within the brain parenchyma. The KWIC reconstructed dynamic curves for AIF, VOF, and tissue density signals were compared to those by the full dose FBP reconstructions using least squares linear regression.

3.4 Results

3.4.1 Simulated FORBILD Phantom CTP Data

The reconstructed images of the FORBILD head phantom using the full dose FBP and KWIC with different dose reduction levels (100, 50, 25, 12.5%) are shown in Fig. 3-4a. The quality of FBP reconstructed images is degraded by streaking artifacts (blue arrows) at reduced dose levels, while the streaks are drastically reduced in KWIC reconstructed images down to 12.5% dose level. A numerically simulated time-varying object (red arrow in Fig. 3-4, 5mm size) for CTP is clearly visible at all dose reduction levels for FBP and KWIC (10mm and 50mm objects are not shown because they were separate simulations with the object in the same place). At 12.5% dose the FORBILD resolution fiducials (white arrows) are barely visible in the FBP reconstructed images while they are still detectable in KWIC reconstructed images. Figure 3-4b shows the gamma variate signal curves from the 5mm object using FBP and KWIC reconstructions down to

12.5% dose. The KWIC reconstructed signal curves down to 12.5% dose are virtually equivalent

to that of the full dose FBP reconstruction.
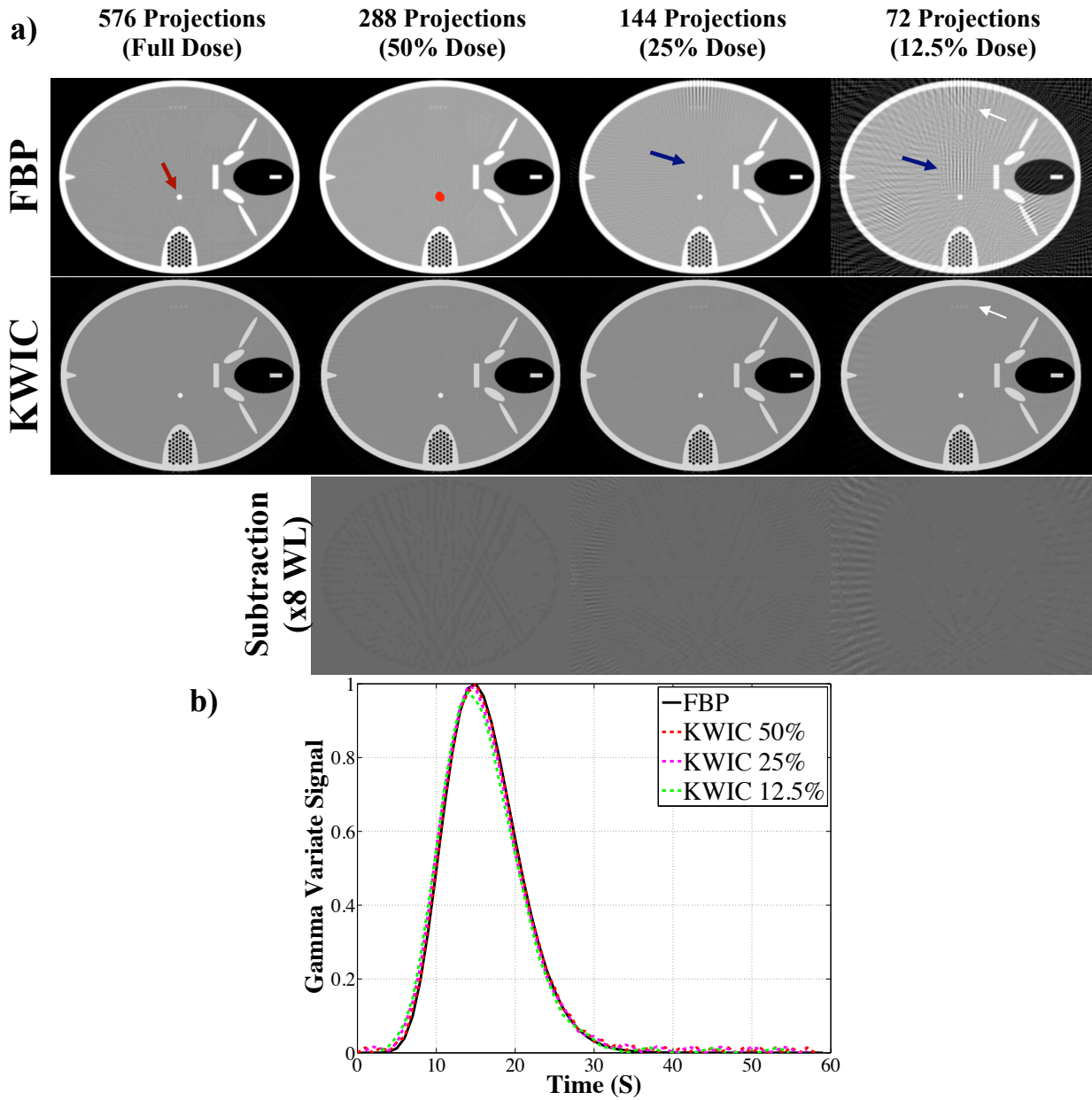
Figure 3-4 FORBILD CT phantom, a), with a 5mm object (red arrow) reconstructed using FBP and KWIC. Streaking artifacts (blue arrows) are present in FBP but not KWIC reconstructed images down to 25% dose level. The resolution fiducials (white arrows) are still visible at 12.5% dose in the KWIC reconstruction while in the FBP they are not visible. The red dot is the ROI drawn to obtain the dynamic curve of the time-varying object. The subtraction images show the artifacts from the KWIC. The gamma variate dynamic time curve, b), is similar at all dose reconstruction levels.

In Table 3-2, the FWHM, TTP, and AUC measurements show that FBP and KWIC reconstructions are comparable for simulated objects of 5mm, 10mm, and 50mm in size. The largest variation occurs at 12.5% dose KWIC reconstruction, however the normalized root-mean-square error (NRMSE) of the AUC between 12.5% KWIC and FBP is 0.07. The NRMSE of the AUC between 50% KWIC and FBP and 25% KWIC and FBP is 0.04 and 0.05 respectively. The maximum temporal blurring occurred at 50% dose reduction with 0.02s increase in the FWHM.

	FBP Full	KWIC 50%	KWIC 25%	KWIC 12.5%
TTP(s)				
5mm	15	15	14	14
10mm	15	15	15	14
50mm	15	15	15	15
AUC				
5mm	0.0253	0.0310	0.0285	0.0294
10mm	0.0253	0.0271	0.0271	0.0264
50mm	0.0253	0.0270	0.0271	0.0272
FWHM (s)				
5mm	10.712	10.732	10.729	10.696
10mm	10.712	10.705	10.703	10.785
50mm	10.712	10.712	10.712	10.708

Table 3-2 Measure TTP, AUC, and FWHM for numerically simulated time varying object near the middle of the phantom

The time-varying object (red arrow) and the ROI (red dot) drawn are shown in figure 3-5. The subtraction image shows that there are streaking artifacts most prominent near the back of the FORBILD head phantom. At 12.5% of the original dose there is presence of temporal blurring the in subtraction images (blue arrow), and is more prominent in 6.25% of the original dose image.

a)

| 288 Projections (50% Dose) | 144 Projections (25% Dose) | 72 Projections (12.5% Dose) | 36 Projections (6.25% Dose) |

KWIC

Subtraction (x8 WL)

b)
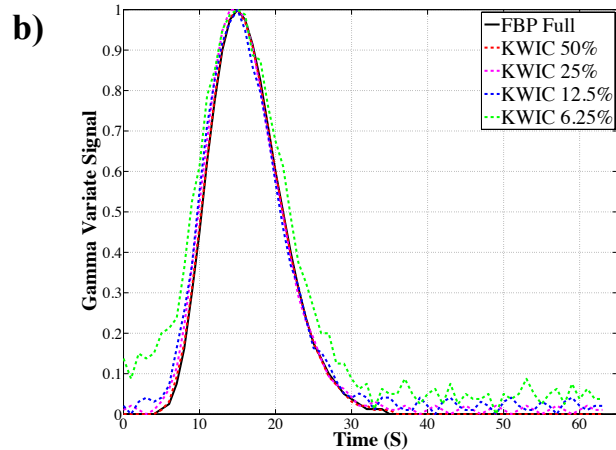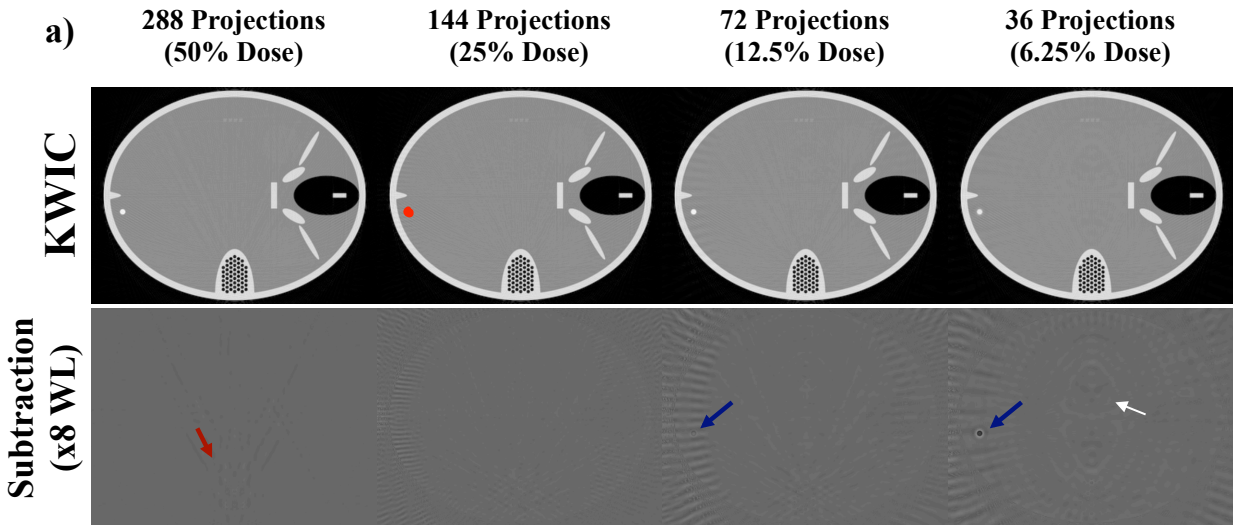
Figure 3-5 FORBILD CT phantom, a), with a 5mm object near the back edge of the phantom. The subtraction images show the artifacts from the KWIC. The red dot is the ROI drawn to obtain the dynamic curve of the time-varying object. Streaking artifacts (red and white arrows) where the time-varying object are seen and introduce more noise into the time curves. The blue arrows identify a temporal blurring artifact due to higher amounts of view sharing at 12.5% and 6.25% KWIC.The gamma variate dynamic time curve, b), is similar at all dose reconstruction levels, except at KWIC 6.25%.

Table 3-3 shows that there is not a significant difference in the measured TTP, AUC, and FWHM up to 12.5% of the original dose despite the streaking artifacts. However, at 6.25% dose the measured AUC, TTP, and FWHM vary about 30-40% compared to the corresponding FBP measurements. The maximum temporal blurring occurred at 6.25% dose reduction with 2.3s increase in the FWHM.

5mm	FBP Full	KWIC 50%	KWIC 25%	KWIC 12.5%	KWIC 6.25%
TTP(s)	15	15	14	15	15
AUC	0.0253	0.0254	0.0270	0.0280	0.0354
FWHM (s)	10.714	10.731	11.022	10.914	13.054

Table 3-3 Measure TTP, AUC, and FWHM for numerically simulated time varying object near the back edge of the phantom

3.4.2 Clinical CTP Data

Figure 3-6 shows the CTP images reconstructed using FBP and KWIC with 50%, 25%, and 12.5% dose levels for one of the 3 *clinical* cases. All CTP images of the KWIC reconstructions are comparable to that of the full dose FBP reconstructions, however at 12.5% dose there are some streaking artifacts. The image quality is significantly improved using KWIC compared to FBP at lower doses, with identifiable brain structures and blood vessels. At 25% and 12.5% dose the FBP reconstructed images are not viable for diagnostic imaging. In the 50% and 25% dose KWIC images, the blood vessels are better delineated mostly due to the windowing and leveling of the images. Due to reconstruction method differences between FBP and KWIC (i.e. kernel size), the images do not have the same signal-to-noise ratios and thus comparable contrast in the images can be difficult to achieve. Also the kernel used in FBP could smooth out finer structures compared to KWIC reconstruction. Difference images between the KWIC images and full dose reconstructed images (bottom row). The window and leveling was increased by x8 to show the difference. The noise becomes more grainy as the dose reduction increases, and there are visible streaking artifacts near the edge of the head.
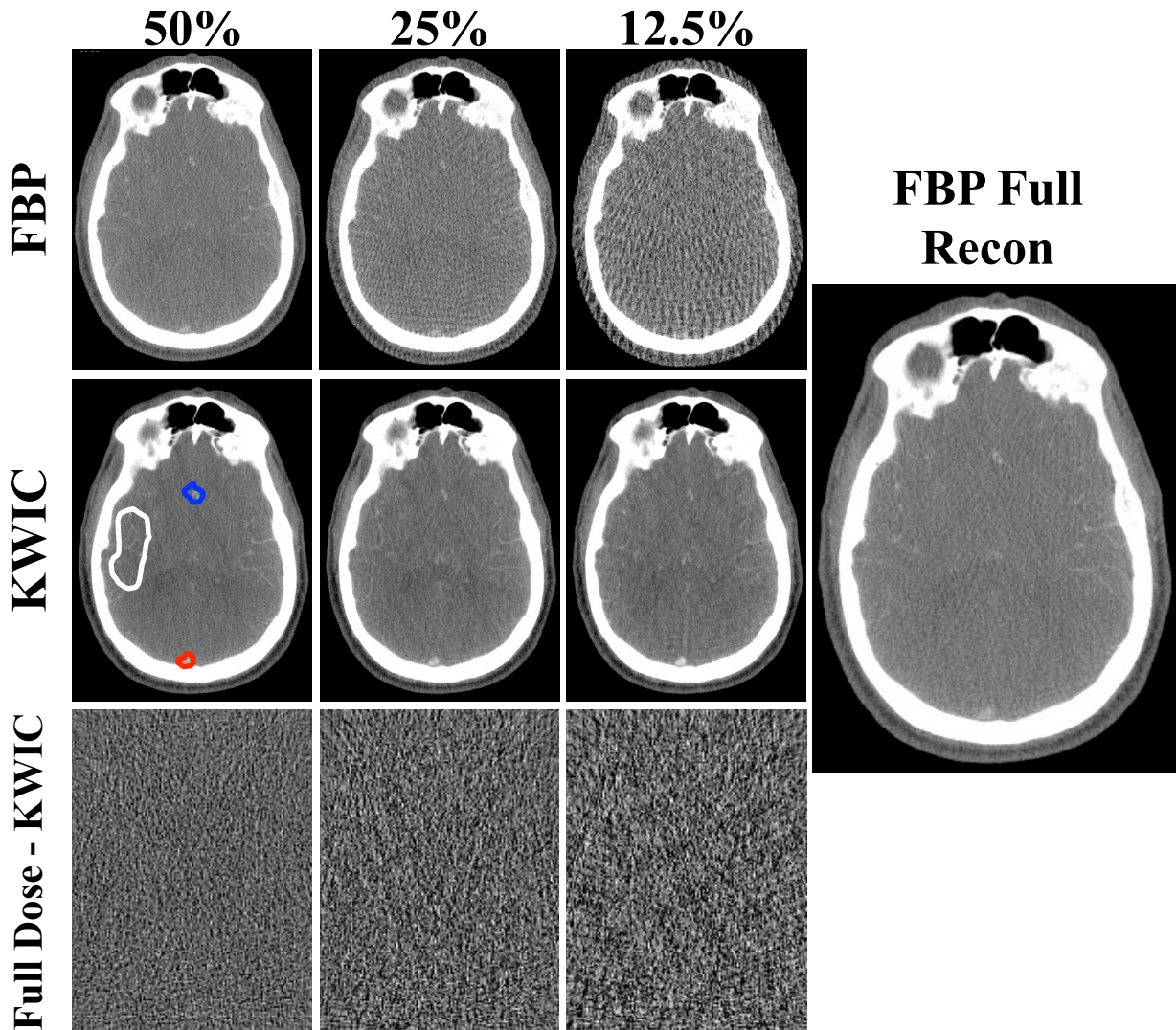
Figure 3-6 FBP and KWIC reconstructed STP cases at 50%, 25%, and 12.5% dose levels. The image quality shows slight degrading in the KWIC reconstructions while the FBP images show a greater increase in streaking artifacts as the dose reduction increases. Difference images between the KWIC images and full dose reconstructed images (bottom row). The window leveling (WL) and width (WW) was decreased by x8 to show the difference (WL: 67, WW: 1800). The window leveling and width for the FBP and KWIC images are 11000 and 8500, respectively. (The noise becomes more grainy as the dose reduction increases, and there are visible streaking artifacts near the edge of the head. The white, blue, and red ROI's are where the ROI's were drawn to generate tissue, arterial, and venous time curves. The white ROI was also used to measure CBF and CBV in the tissue.

The AIF, VOF, and tissue density signals are shown in Figure 3-7 for FBP and KWIC

reconstructions respectively. The signal curves from the KWIC reconstructions down to 25%

dose level are virtually identical to those of FBP. However, slight deviation is observed for the

12.5% dose KWIC curves compared to the reference curves of FBP. The scatter plots of figure 3-8 further show the strong correlations between the full dose FBP signals and those by KWIC reconstructions for AIF, VOF and tissue density curves respectively. The maximum temporal blurring between all three CTP cases occurred at 12.5% dose reduction for case 2 with 0.5s increase in the FWHM.
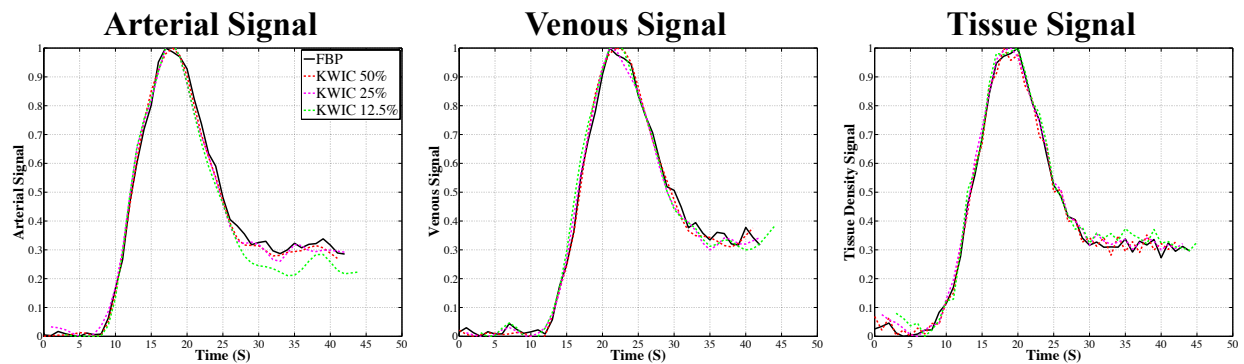
Figure 3-7 Dynamic contrast curves for arterial, venous, and tissue ROIs generated with FBP full dose reconstruction, 50%, 25%, and 12.5% KWIC reconstruction. The noise in the signal minimally increases as the dose reduction increases.
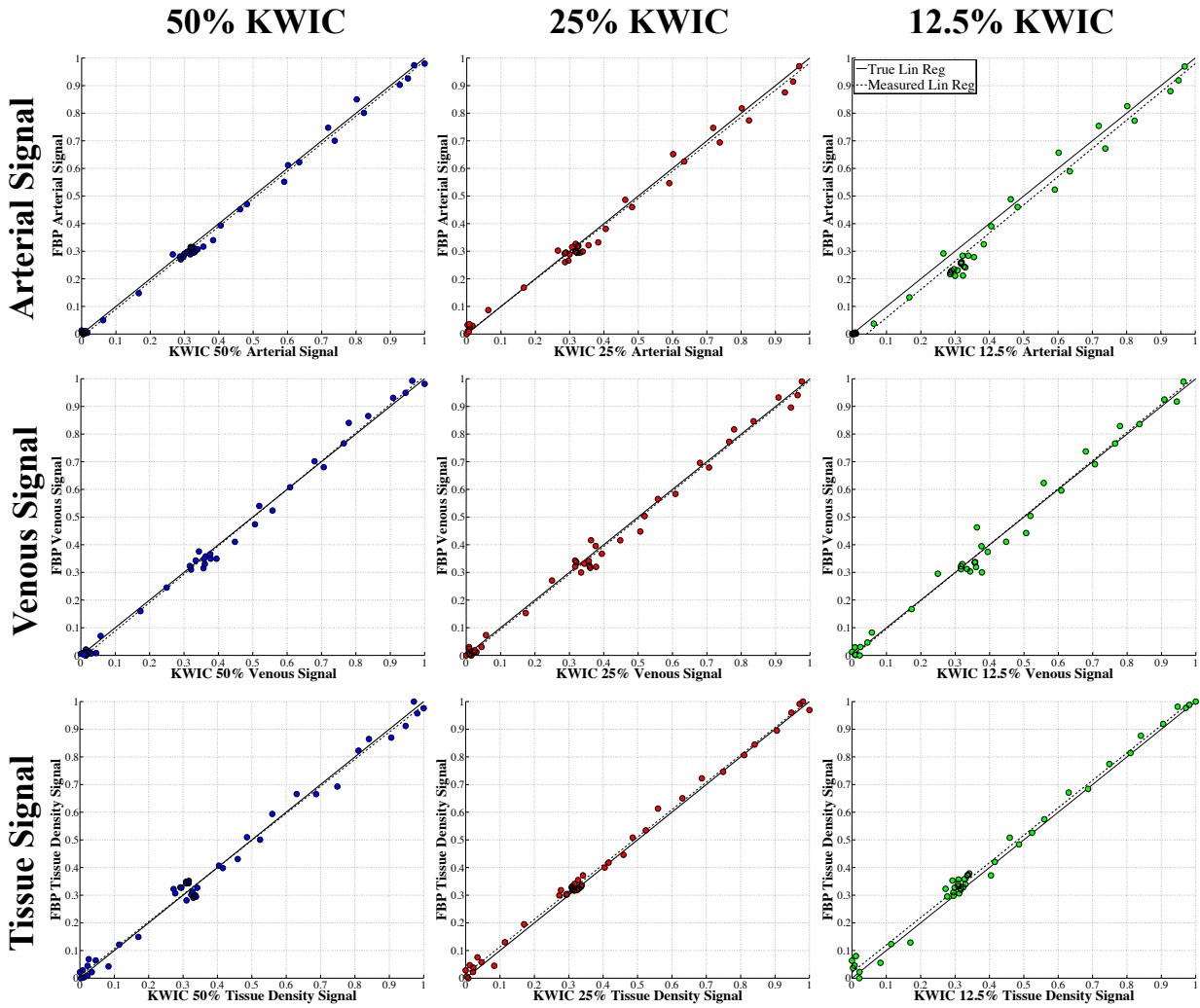
Figure 3-8 Correlation plots for Arterial (first row), Venous (second row), and Tissue (third row) signal curves comparing FBP and the KWIC reconstruction. There is high correlation at all dose reconstruction levels.

Figure 3-9 shows the quantitative CBF maps for one of the clinical CTP cases (case 3). The CBF maps generated with KWIC reconstructions are comparable to those by full dose FBP. However, some variations of CBF maps can be observed across different dose levels, e.g., the CBF maps of full radial and 12.5% KWIC have a lower intensity compared to full dose FBP and 50% and 25% KWIC CBF maps. Table 3-4 shows the measured CBF and CBV in the motor cortex region of the brain. There is no significant difference of CBV and CBF values between

KWIC and FBP reconstructed images. The quantitative perfusion metrics (CBF and CBV) are not significantly different (p>0.05) between FBP and KWIC reconstructions (only CBF maps are shown).
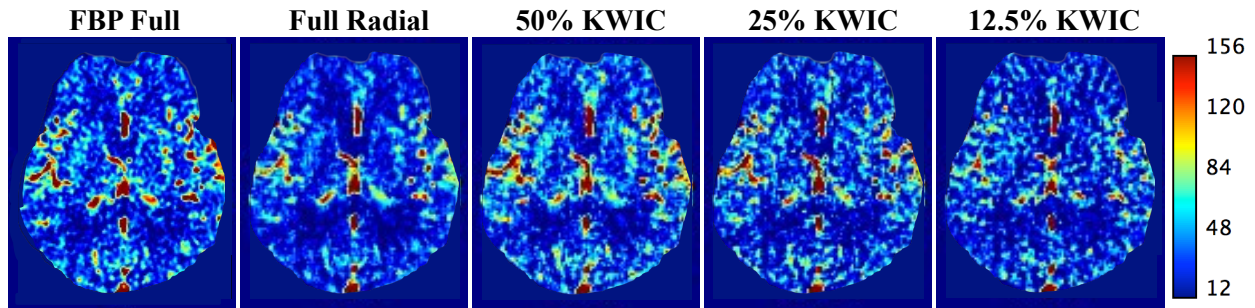
Figure 3-9 CBF maps generated from a clinical case using FBP and radial gridding with all projections (Full Radial), KWIC reconstruction at 50%, 25%, and 12.5% dose reduction levels. The CBF maps of full radial and 12.5% KWIC have a lower intensity compared to FBP full and 50% and 25% KWIC CBF maps.

	FBP Full	Full Radial	KWIC 50%	KWIC 25%	KWIC 12.5%
CBF(ml/100g/min)					
Case 1	40.4 ± 30.3	34.5 ± 26.6	42.8 ± 33.2	51.0 ± 52.7	46.3 ± 40.3
Case 2	49.1 ± 23.2	33.0 ± 15.9	53.1 ± 32.1	52.6 ± 31.8	52.5 ± 38.7
Case 3	56.9 ± 37.9	51.48 ± 33.2	65.5 ± 39.2	59.0 ± 37.2	49.7 ± 29.0
CBV (ml/100g)					
Case 1	6.4 ± 3.2	5.2 ± 3.1	5.6 ± 3.4	6.7 ± 4.2	6.5 ± 3.6
Case 2	7.9 ± 2.7	5.3 ± 2.1	6.1 ± 2.7	6.4 ± 3.2	7.4 ± 4.1
Case 3	7.9 ± 4.3	6.8 ± 3.3	6.9 ± 3.5	6.9 ± 3.6	6.7 ± 3.2

Table 3-4 Measured CBF and CBV values for all cases. ROI was drawn in the motor cortex region.

3.5 Discussion

In both the simulated and clinical CTP data, KWIC was able to reduce the radiation dose down to 25% of the original dose without significantly affecting the image quality and perfusion quantification. While the original goal of KWIC was for preserving spatial and

temporal resolutions in accelerated 4D dynamic MRI, its application in dynamic CT scans results in a reduced number of total X-ray projections required per gantry rotation. Coupled with fast X-ray switching and a custom acquisition scheme, it is foreseeable that perfusion exams could be conducted at reduced total radiation doses. This innovation builds on the central-slice theorem that relates the CT sinogram to "k-space" data by performing 1-D FT of the projection of an object, which is the same as the line drawn through the center of the 2-D FT plane (i.e., k-space). Therefore many algorithms developed for accelerated dynamic MRI including KWIC can be adapted for low dose dynamic CT scans such as CT perfusion and angiography[29,62,75]. The drawback of KWIC is potential temporal blurring of fine objects comprising primarily high spatial frequencies. Based on our simulation, however, there is no apparent temporal blurring of CTP time courses for objects as small as 5mm in size. Clinical CTP data did not show temporal blurring of the AIF, VOF or tissue density curves. While our initial goal is to reduce the radiation dose of brain CTP, the technology can be expanded to CTP of body organs, which is rarely performed due to excessive radiation dose. Our technique may also be adapted for multiphase CT angiography (CTA) of the brain and heart. One of the limitations of CTA in clinical applications is that the peak of the contrast bolus might not be precisely captured leading to either rescanning of the patient or misdiagnosing the disease[76]. With CT KWIC more time points can be acquired with the same amount of dose, and thus improving the quality and reliability of CT angiography scans.

In the present study, KWIC was able to reduce the radiation dose down to 25% of the original dose without compromising the image quality of simulated CTP and clinical CTP cases without head motion (case 3). However, in the clinical case presenting head motion the

achievable dose reduction was ~50% (case 1 and 2). Since the higher frequency k-space regions are shared between neighboring time frames in KWIC, the effect of sudden head motion is propagated to neighboring time frames during reconstruction, affecting the final image quality. While motion was observed to have an impact on reconstruction quality and dose reduction potential, other studies[30,77] have proposed methods for auto-detection and correction of motion in radial projection acquisitions that would be applicable to the KWIC methods utilized in this work. In the present study, we observed some variations in CBF maps generated across different dose levels (Fig. 9), which may be attributed to variations in the hand drawn ROI's for the VOF and AIF, as well as different amount of view sharing, or potential patient motion. However, there was no significant difference in the measured ROI values (Table 3-4). Detailed investigation into the effects of motion on KWIC reconstructed CTP as well as its correction await further investigation in future studies.

Besides the angle-bisection scheme employed in the present study, alternative sampling sequences may be applied for KWIC such as the golden ratio scheme in which the rotation angles of the X-ray source are spaced by the golden angle (180°/1.618 = 111.25°). The golden ratio scheme guarantees an optimal projection distribution for any arbitrary number of projections used in reconstruction, especially if the number of total projection views is a Fibonacci number[31,71,78]. To improve the sampling efficiency, a "tiny golden angle" scheme was introduced recently based on a generalized Fibonacci sequence that allows a smaller angle increment while still maintaining the sampling efficiency as the standard golden angle scheme[71,78]. It is worth noting that as a pseudo-random sequence, the (tiny) golden ratio scheme

is also ideal for modern sparse sampling techniques with constrained reconstruction such as compressed sensing (CS).

The main competition of KWIC is iterative reconstruction (IR) algorithms currently offered by all major CT vendors. Disadvantages of IR potentially include blotchy image appearance and longer computational time. As mentioned, clinical application of IR for CTP has been very limited due to the high complexity and computational burden for processing dynamic CTP images that impairs clinical workflow. In contrast, KWIC does not prolong reconstruction time and is computationally comparable to FBP. Furthermore, our technology is not exclusive to existing low dose CT technologies, and can be combined with IR to dramatically reduce radiation dose of existing CT scans.

Another similar study in reducing the radiation dose by retrospectively reducing the number of projections used is HYPR[62,63]. HYPR uses the assumption that the image is a product of the composite image (all projections) and a weighting factor in the image domain. HYPR additionally convolves a low-pass filtering kernel to smooth out the streaking artifacts in the retrospectively undersampled low dose image. The main difference between HYPR and KWIC is the weighting mechanism. HYPR uses a high-quality composite image of all the projections from the dynamic series to generate low-noise image frames with high spatial and temporal resolutions. KWIC uses view sharing from immediate neighboring time points in the frequency domain (i.e., local k-space filter) to minimize streaking artifacts to generate dynamic images with high spatial and temporal resolutions. While HYPR can improve the noise and spatial resolution of the dynamic images, residual artifacts can still occur[79,80]. Additional methods may be required

to mitigate these artifacts[81]. If there is patient motion this can lead to streaking artifacts across all the HYPR images. KWIC reconstruction is also susceptible to streaking motion artifacts, however the streaking artifacts are limited to the images with motion while HYPR is susceptible to motion artifacts across the dynamic series due to the composite weighted image. HYPR also uses a smoothing kernel and can decrease the spatial resolution of the images, which can affect the perfusion quantification in regions with smaller blood vessels. KWIC does not decrease the spatial resolution because it is sharing information in neighboring time points and does not require the smoothing kernel as HYPR does.

A limitation of the KWIC algorithm is that due to the view-sharing in the higher-spatial frequencies there will be inherent temporal blurring. It has been shown in this study as well as in MRI KWIC studies[11,12] that the effects of temporal blurring are minimal when the projection undersampling (e.g. dose reduction) is less than 75%. The temporal blurring of the contrast uptake is more significant with smaller features (e.g. higher spatial frequencies)[11] because of the higher amounts of view sharing. The temporal blurring can lead to CT number discrepancies in areas where there is contrast uptake. If there is patient motion the angle bisection acquisition of the projections can lead to streaking artifacts. Using CS for the undersmapled projections is a promising technique to reduce the streaking artifacts without view-sharing, which would reduce the streaking artifacts due to motion and potentially improve the CTP metrics[75]. Also due to the interleaved view sharing there is a discontinuity in the projections in the KWIC reconstruction that can lead to streaking artifacts, when there are a higher number of sub-apertures used. Previous KWIC studies[11,12,82] and this study show that using 8 sub-apertures is the upper limit before reconstruction artifacts are unacceptable.

KWIC does require sparse sampling through high speed X-ray switching, which could theoretically be implemented using hardware and/or software approaches. Grid controlled X-ray tube is an existing technology that allows pulsed X-ray on a very short time scale (micro to milliseconds). It has been applied for pulsed fluoroscopy to reduce radiation dose[83]. Grid-controlled X-ray has also been applied for flying focal spot CT to rapidly shift the focal spot of electron beam as a means to increase the slice coverage or resolution[84]. Therefore, it could be feasible to adapt grid-controlled X-ray for pulsed CT acquisition as required by KWIC. Currently there are organ based tube current modulation techniques that have very rapid changes in mA and are clinically used[85]. Alternatively, mechanical approaches such as a lead shutter may be applied for implementing pulsed X-ray. Software control of intensity-modulated X-ray has been applied for CT with reduced radiation dose, e.g., for thoracic imaging to spare lung/breast and cardiac imaging to focus on specific cardiac phases, although the time scale of existing X-ray intensity modulation is generally on the order of a few hundred milliseconds. Both hardware and software approaches can be explored for the implementation of pulsed X-ray in future studies. We recognize that the potential hardware developments required to implement the proposed CTP acquisition/reconstruction approach are substantial, however the work presented demonstrates the compelling dose-reduction benefits that could be possible with such technology, and the potential new applications of low-dose CTP, that such hardware developments would enable, could be a powerful pathway for improvements in clinical care.

3.6 Conclusions

In this work, we presented a low dose CTP technique by adapting a projection view-sharing technique named KWIC that was originally developed for accelerated 4D dynamic MRI with radial trajectories[11,12]. This study provides a proof-of-concept for KWIC reconstruction of CTP to achieve ~75% dose reduction without compromising imaging speed or quality. With high speed X-ray switching, this technique may be expanded for CTP of body organs and multi-phase CTA as well as to include other constrained sparse sampling techniques. Future work will concentrate on further improvement of SNR of the KWIC reconstruction with CT data, further validation of the proposed algorithm in clinical CTP studies, and addressing sampling requirements of the acquisition schemes via new sampling protocols (e.g. tiny golden angle) and hardware and software developments to achieve the required fast X-ray switching. As demonstrated, KWIC's potential for use in CTP provides another possible pathway to reduce the radiation dose of current CT perfusions exams as well as possible pathways towards clinical body perfusion with CT, and reduced-dose CT angiography.

4 MRI CHARACTERIZATION OF UTERINE MOTION IN EARLY GESTATION USING IMAGE-BASED MOTION TRACKING

4.1 Introduction

Placental function and growth is critically important to fetal health and growth [86–88]. Ultrasound is the primary technique for imaging the fetus and placenta primarily because of its proven utility, easy accessibility, and the low cost compared to other imaging modalities. However, the limitations of ultrasound include soft-tissue contrast, small field of view (cannot measure placenta volume), and poor image quality in some placental functional imaging, which makes ultrasound findings potentially inconclusive or insufficient to guide treatment options [89]. MRI is a promising technique because it provides great tissue contrast, functional imaging, and there is no ionizing radiation [90]. However, motion in MRI still remains one of the major limiting factors.

The motion of the placenta and uterus can be caused by multiple factors, including uterine contractions, maternal respiration, fetal motion, and other organ motion [8,9]. In particular, uterine contractions can compress the superior region of the uterus, causing significant motion in the uterus and placenta. The extent these sources of motion should be accounted and adjusted for in MRI imaging has not been well studied. Dickinson et al. studied the uterine contraction activity during gestational ages (GA) of 20 weeks – 40 weeks and showed that there is a mean contraction frequency in pregnant women of ~2 contractions/hour [10]. They also concluded that the frequency and magnitude of contractions increase steadily throughout gestation. Though the study provides the frequency, duration, and magnitude of uterine contractions, measurements were conducted from an external source. Further, the direction of contractions or the magnitude of the direction, which can affect the imaging technique in MRI was not forthcoming. Another study revealed uterine contractions to demonstrate a graded response on the fetal heart rate suggesting that uterine contractions may pose a physiological challenge to the developing fetal cardiovascular system [91]. This study used monitors recording electrophysiological signals of the fetal heart electrocardiogram (ECG) and uterine contractions by the electrohysterogram (EHG). However, only about 70% of the time was the fetal heart rate accurately measured and the EHG reported 19% false positive detection of uterine contractions. Using MRI imaging can potentially reduce false positive detection of uterine contractions, related to direct visualization of uterine and fetal activity.

Recently a 3D stack of stars golden angle radial gradient echo sequence was developed to generate more motion robust images and provide a self-gated signal [7,27,30,32–35]. Having this

image sequence can provide 3D dynamic images of the uterus and thereby provide accurate temporal and magnitude information about uterine activity. Additionally, Wu et al. [92] developed an image based motion tracking algorithm that uses dynamic images that track cardiac motion improving motion compensation towards better visualization of the coronary arteries. This algorithm is applicable to any dynamic set of images, including the uterus, providing spatial and temporal information.

In this study, we implemented an image-based template matching algorithm for tracking uterine motion based on 3D dynamic images reconstructed by k-space weighted image contrast (KWIC) [11,12]. This algorithm generates motion time plots of the uterus in the superior/inferior (SI) and left/right (LR) directions. Uterine contraction and uterine motion caused by maternal motion (e.g. maternal respiration and other maternal organ motion) were separated based on the uterine motion time plot. Using the motion information we aim to characterize uterine contraction and maternal motion in terms of direction and duration. Associations with gestational age, fetal sex, and placental position will also be investigated in the case of uterine contraction and maternal motion.

4.2 Methods

4.2.1 Study Population

UCLA's Institutional Review Board (IRB) approved this prospective study. Sixty-one pregnant women (mean age: 35 ± 5 years, range: 22-45 years) were consented and recruited from UCLA's antenatal clinics for a placental MRI study. Forty-eight of the subjects were scanned twice at two

different gestational ages during their second trimester, with the first scan between 14 - 18 weeks, and the second scan between 19 - 24 weeks. The other 13 subjects underwent only their first MRI (14-18 weeks gestation age) as they voluntarily withdrew from the study. In total there were 109 MRI exams. The inclusion criteria for the subjects were the clinical confirmation of pregnancy, and exclusion criteria consisted of any known pregnancy abnormalities at the time of recruitment. There were only three subjects who either developed preeclampsia or presented subsequently with intrauterine growth restriction (IUGR). Since these subjects delivered babies later with no immediate morbidity, we did not exclude them from our present study, which was performed during the second trimester.

4.2.2 MRI techniques and Reconstruction

All MRI exams were performed on two 3T scanners (Prisma and Skyra, Siemens Healthcare, Erlangen, Germany) using a body array coil. Subjects were positioned feet-first supine. A T2-weighted scan was performed using T2-HASTE sequence to get an anatomy scan of the abdomen/pelvis region. This was used to identify the placenta, uterus, and other relevant anatomy. A 3D multi-echo golden angle radial gradient echo (GRE) sequence was used for assessment of uterine contractions and maternal motion. The first echo was used for reconstruction because, on average, it had the best qualitative contrast of the placenta, uterus, and fetus. There were two main protocols used for the sequence and are listed in table 4-1. Using golden angle rotation of the radial acquisition allows for retrospective flexibility of the temporal and spatial resolution of the dynamic images that were reconstructed [31]. The first set of data

acquisition only used 6 echoes for data acquisition while later 12 echoes were used. The total

acquisition time for the 6 echo scans was 4-5 min and for the 12 echo scans it was 5:30-6 min.

Imaging Parameters	GA Radial GRE (a)	GA Radial GRE (b)
Number of Echoes	6	12
TE_1 (ms)	1.23	1.23
ΔTE (ms)	1.23	1.23
TR (ms)	8.85	15.9
Matrix Size	160 x 160 x 32-48	224 x 224 x 44
FOV (mm^3)	350 x 350 x 168-200	379 x 379 x 154-198
Slice Thickness (mm)	3.5-5	3.5-4.5
Radial Spokes	620	440
Flip Angle (degrees)	5	5
Scan Time (min:sec)	3:18-4:57	5:35-6:06

Table 4-1 Representative sequence parameters for in vivo placenta scans.

A dynamic set of images were reconstructed offline using KWIC [11]. The KWIC

algorithm progressively increases the k-space information from the center of k-space to the outer

region, where the outer region shares the k-space information from other time points (see Fig 4-

1). We used 10 radial spokes in the center of k-space and 170 spokes used in the outer most ring.

For the two acquisition protocols, the temporal resolution was 4.24 seconds and 7.63 seconds.

The images were reconstructed in axial slices and reformatted to coronal and sagittal planes (see

Fig 4-1). The coronal and axial images were used to determine uterine and maternal motion in

SI and LR directions, respectively.
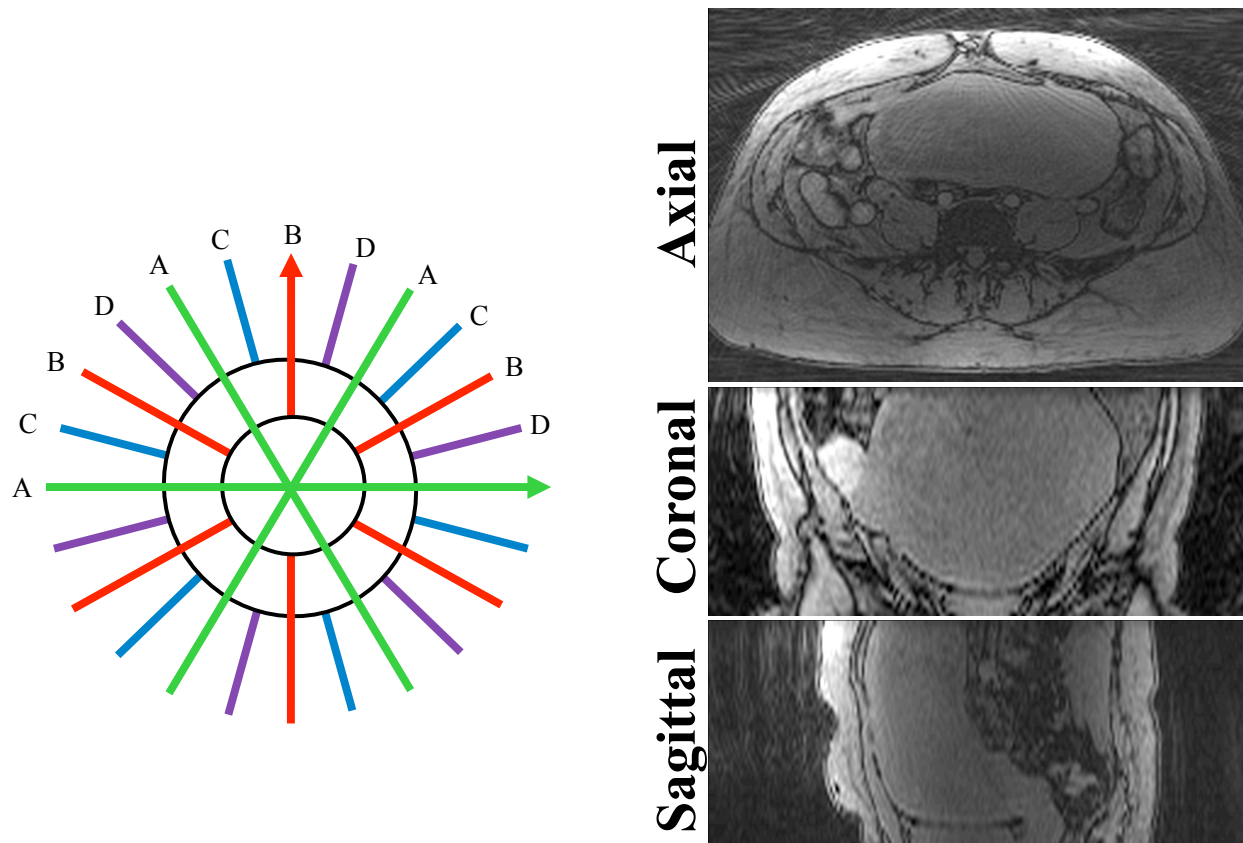
Figure 4-1 Diagram of KWIC reconstruction (left). The 3D reconstruction was used to reformat axial images into coronal and sagittal planes to process SI and LR motion (right).

4.2.3 Image Based Template-Matching Motion Tracking

We used an in-house software developed for tracking the uterine motion employing an image-based template matching algorithm [92]. The uterine motion along the SI and LR directions was measured on 2D coronal and axial images, which covered the uterus, from the 3D dynamic image sets, respectively (Fig 4-2). The inner rectangle (dashed-line) depicts the target region-of-interest (ROI) for tracking, and the outer rectangle (solid line) delineates the search region based on the expected ranges of motion to reduce processing time. The inner rectangle was manually drawn to cover the superior or left/right regions of the uterus, which provided features with better contrast and reduced noise bias. A least-squares error metric based on normalized image intensity was used to determine the position of the target feature at each dynamic time frame.

The initial position of the feature (at the first time frame) was then subtracted from the best-matched target location (minimized error) in the search region to calculate motion coordinates in two directions at each time frame. This algorithm tracks the uterine contractions as well as the uterine motion caused by maternal motion. A multi-resolution of four fold was used for measuring uterine motion at a higher resolution. Fetal motion was not a significant contributor to uterine motion given that the gestational age of the subjects at the time of the MRI scans was less than 26 weeks. The fetus at these early stages of gestation does not demonstrate much movement and is not compressed against the uterine wall as seen later in gestation.

The center-of-mass of the inner rectangle location (x-y coordinate) was determined for each time point. The SI direction of motion was determined by the y-coordinate when motion tracking was performed on coronal images, and the LR direction of motion was determined by the x-coordinate of the center-of-mass when motion tracking was performed on axial images. We then performed motion tracking on multiple coronal and axial slices within the uterus. The center-of-mass location was averaged across all slices within the uterus for each time point to smooth any random fluctuations that may occur while tracking uterine motion. The mean center-of-mass of the inner rectangle was determined for each time point in coronal and axial images resulting in the uterine motion time plot for SI and LR directions as shown in Fig 4-2 (right).
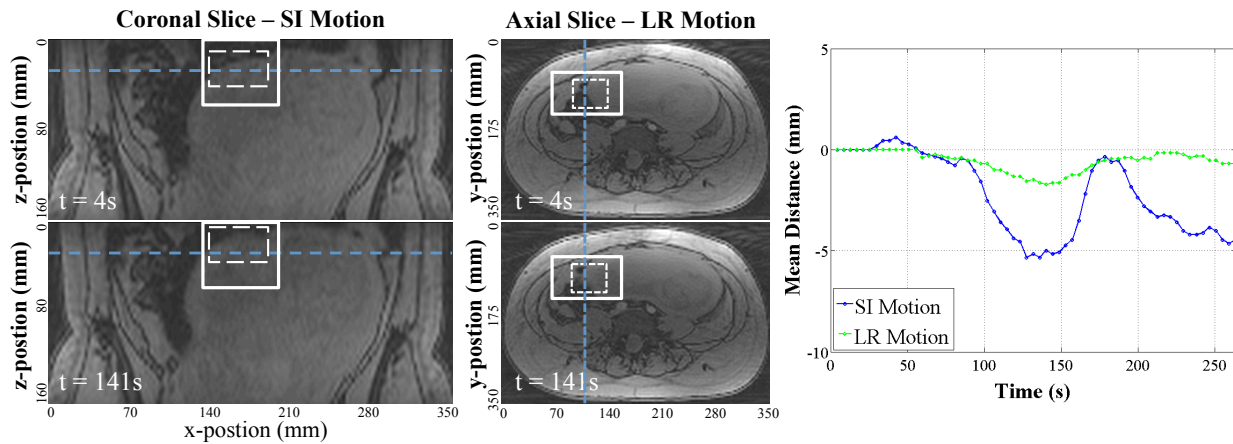
Figure 4-2 Example images and plot of measuring the uterine motion with the image-based template matching algorithm. The coronal reformatted images were used to measure superior-inferior (SI) motion (blue line) and axial images were used to measure left-right (LR) motion (green line). The template matching algorithm searches for the target ROI (dotted white line) within the search region (solid squares) for each dynamic time frame, using a least-squares error metric based on normalized image intensity. Note that the uterine contraction during the scan can be seen in the plot on the right.

4.2.4 Uterine Contraction and Maternal Motion

Uterine contractions were confirmed by an experienced abdominal radiologist (with 10 years of experience) and an experienced maternal fetal medicine specialist (with 20 years of experience). The uterine motion caused by maternal factors refers to all other motion (respiratory, subject, and other organ motion) or situations without contractions and is termed maternal motion. Three studies were excluded from the analysis. Two contractions did not finish before the MRI scan ended, so the full duration of the contraction could not be determined. The other exam was excluded due to significant maternal motion that made it difficult to distinguish between maternal motion and uterine contractions.

The maximum amplitude of the SI and LR (same time point) uterine motion time plot during the scan was used to identify SI and LR directions of the uterine contraction and maternal motion. For uterine contractions, the duration was measured from the start to the finish of contractions in uterine motion time plots.

For uterine contractions, three associations were mainly investigated if there was a significant difference in uterine contractions between (i) gestational age, (ii) sex of the fetus, and (iii) placental location (anterior and posterior [93]). All were in relation to uterine motion in terms of direction and duration. For the gestational age comparison, we assumed that the contractions were independent of each other since there was only one subject having contractions during both scans. For maternal motion, we also investigated if there was a significant difference between (i) gestational age, (ii) sex of the fetus, and (iii) placental location. However, we only used direction, because it was difficult to generalize the duration of maternal motion for each scan. Exams with uterine contractions were excluded due to interference resulting in a potential bias when analyzing maternal motion. Singular value decomposition (SVD) was used on uterine contraction and maternal motion to determine singular values or the dominant direction of motion, as well as the angular direction of motion between SI and LR. There were eight uterine contractions and twenty-three incidents of maternal motion where the fetal sex was unknown, thus were excluded from comparisons in the fetal sex analysis.

4.2.5 Statistical Analysis

The data are presented as mean ± standard deviation, and stratified into three groups: gestational age 14-18 weeks and 19-24 weeks (1st and 2nd MRI, respectively), fetal sex (male and female), and placental location (anterior and posterior). A two-group t-test was performed for uterine contraction related motion, because only one subject had uterine contractions in both MRI scans. For the one subject with contractions in both scans we averaged the duration and the direction values of the uterine contractions, and assumed it as not a mixed model. A paired t-test was performed on the maternal motion for gestational age on thirty-four subjects and an unpaired t-test was performed on the other forty-eight subjects to compare means of fetal sex and placental location. The paired data for gestational age were derived from subjects that underwent both MRI scans and did not have a contraction in either scan (n= 34). A p-value less than 0.05 were considered significant for all statistical analyses. The statistical tests were performed in Microsoft Excel.

4.3 Results

4.3.1 Uterine Contraction

In total 20% (n = 22) of the MRI scans had uterine contractions related to motion. We also observed that uterine contractions occurred 18% of the time during14-18 weeks gestational age and 25% of the time during 19-24 weeks.

Figure 4-3 shows uterine contractions of subjects in their first (green) and second (blue) MRI. With all of the exams combined, SVD shows that the dominant direction was SI (top row),

as well as in the 1st MRI and 2nd MRI scans. The dominant direction of motion was SI (see Table 4-2) when comparing between LR and SI motion in the 1st MRI (p = 0.04) and 2nd MRI (p = 0.0003). The mean duration of the contractions related to motion for the 1st MRI was 151.4s ± 23.4s and for the 2nd MRI was 124.9s ± 28.0s. It was observed that there was a statistically significant difference (p = 0.034) between the duration of these contractions between the 1st and 2nd MRI. The mean duration was greater for the 1st MRI (151.4 ± 23.4 seconds) compared to the 2nd MRI (124.9 ± 28.0 seconds).
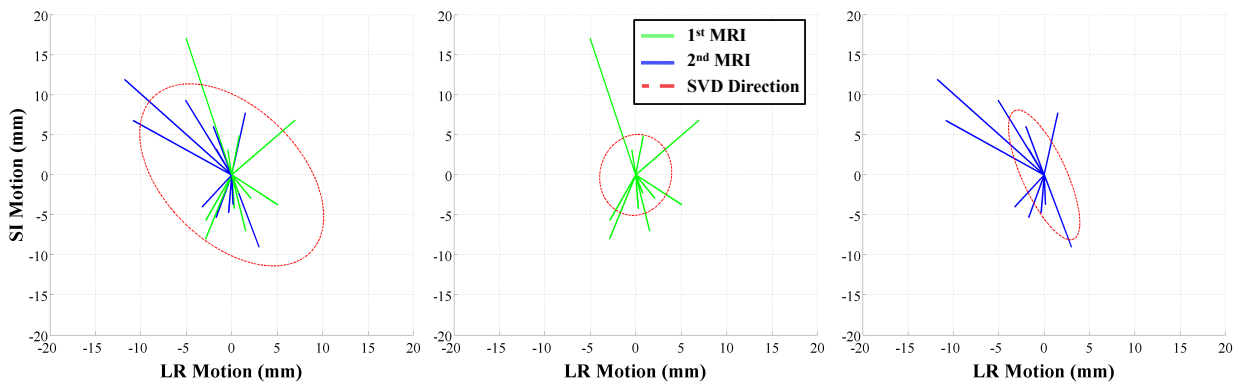
Figure 4-3 Uterine contraction for patient's 1st (green) and 2nd (blue) MRI and represents the SI and LR motion. The SVD demonstrates the dominant direction of motion for SI and LR directions.

The uterine contractions between male (green) and female (magenta) fetal sex are shown in Figure 4-4. The SVD shows that the dominant direction was SI (top row) for combined and separate comparisons of male and female fetuses. We observed a significant difference between LR and SI motion for female (p = 0.025) and male (p = 0.005). The mean duration was significantly greater for male fetuses (p = 0.044).
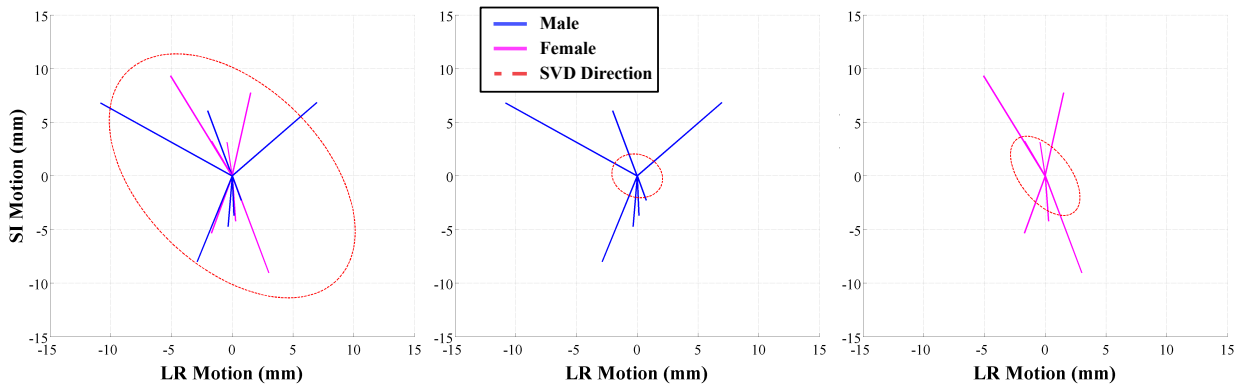
Figure 4-4 Uterine contraction for male (blue) and female (magenta) fetuses and shows the SI and LR motion. The SVD demonstrates the dominant direction of motion between SI and LR directions. The dominant direction of motion is SI.

The placental location (anterior and posterior) in relation to contractions with motion is shown in Figure 4-5. Similar to the fetal sex and gestational age the dominant direction was SI compared to LR motion for both anterior (p = 0.04) and posterior (p = 0.03) positioned placentas. There was no significant difference between the anterior and posterior placental location in terms of direction and duration (see table 4-2) for contraction related motion.
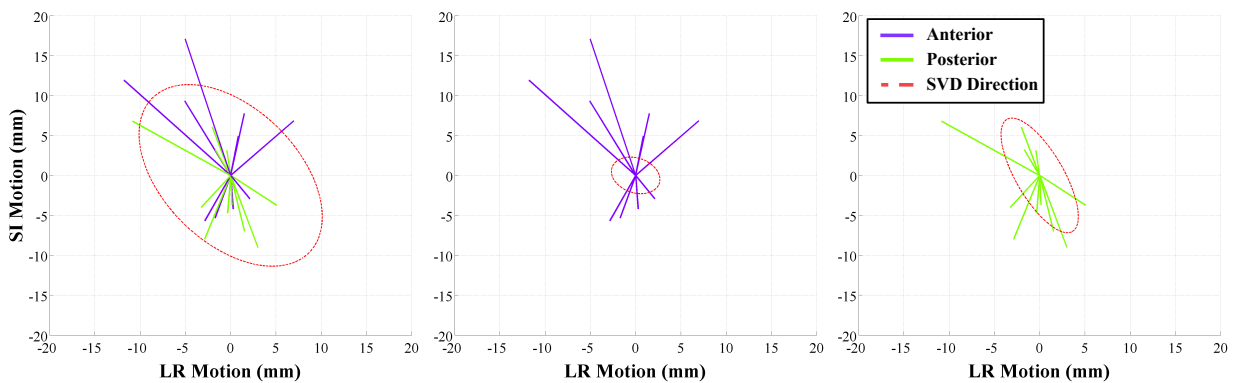
Figure 4-5 Uterine contraction for anterior (magenta) and posterior (green) placental locations. The SVD shows that the dominant direction of motion is SI.

68

		SI (mm)	p-value	LR (mm)	p-value	Duration (sec)	p-value
Uterine Contraction Cases							
Longitudinal	**1st MRI (n = 11)**	6.0 ± 4.1	0.099	2.6 ± 2.2	0.413	151.4 ± 23.4	0.034
	2nd MRI (n = 11)	6.5 ± 2.7		3.7 ± 4.0		124.9 ± 28.0	
Fetal Sex	**Male (n = 7)**	5.5 ± 2.0	0.69	3.4 ± 4.0	0.392	141.7 ± 20.1	0.044
	Female (n = 7)	6.0 ± 2.7		2.0 ± 1.6		106.9 ± 43.2	
Placental Position	**Anterior (n = 10)**	7.6 ± 4.2	0.095	3.8 ± 3.5	0.412	129.8 ± 46.1	0.807
	Posterior (n = 12)	5.1 ± 2.2		2.7 ± 3.0		133.56 ± 23.6	
All Cases		6.3 ± 3.4		3.2 ± 3.2		131.9 ± 34.7	

Table 4-2 Mean motion of SI and LR directions and duration of uterine contraction.

4.3.2 Maternal Motion

Figure 4-6 shows maternal motion for the subjects 1st MRI (green) and 2nd (blue) MRI scans. The SVD (red eclipse) shows that the dominant direction was SI when scans were combined, and separated individually as in the 1st MRI and 2nd MRI. The paired t-test showed that there was a significant difference for LR motion between the 1st and 2nd MRI (p = 0.0001). However, there was no statistically significant difference in the direction of motion, which was SI between the 1st and 2nd MRI (p = 0.44, see table 4-3).
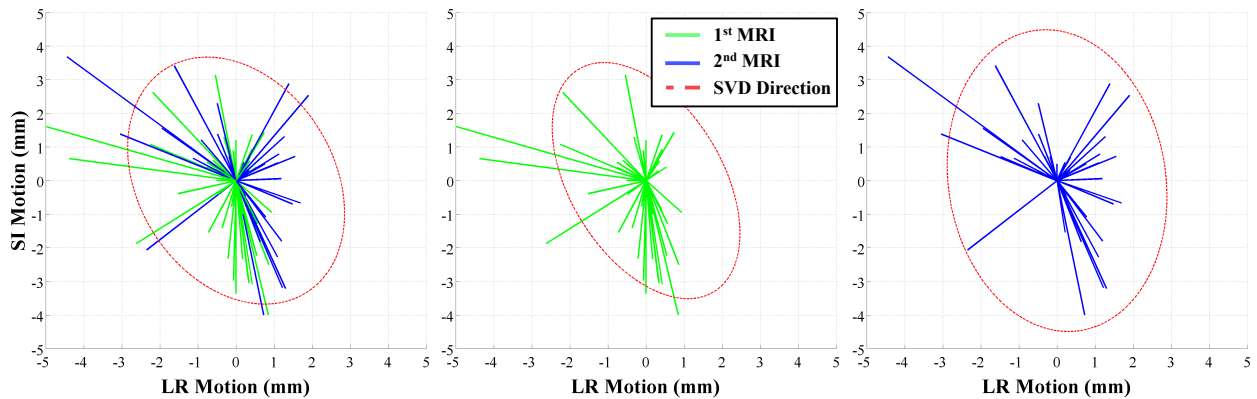
Figure 4-6 Maternal motion for patient's 1st (green) and 2nd (blue) MRI. The SVD shows that the dominant direction of motion is SI.

Figure 4-7 shows the SI and LR motion for maternal motion related to fetal sex. The SVD (red eclipse) shows that the dominant direction was SI for the combined fetal sex, as well as when separated as male and female. There was no significant difference between the LR and SI motion for female fetuses (p = 0.11, see table 4-3), as well as between the female and male for LR (p = 0.54) and SI (p = 0.91) motion. There was however statistically significant difference (p = 0.01) noted in the direction of motion between the LR and SI for male fetuses alone.
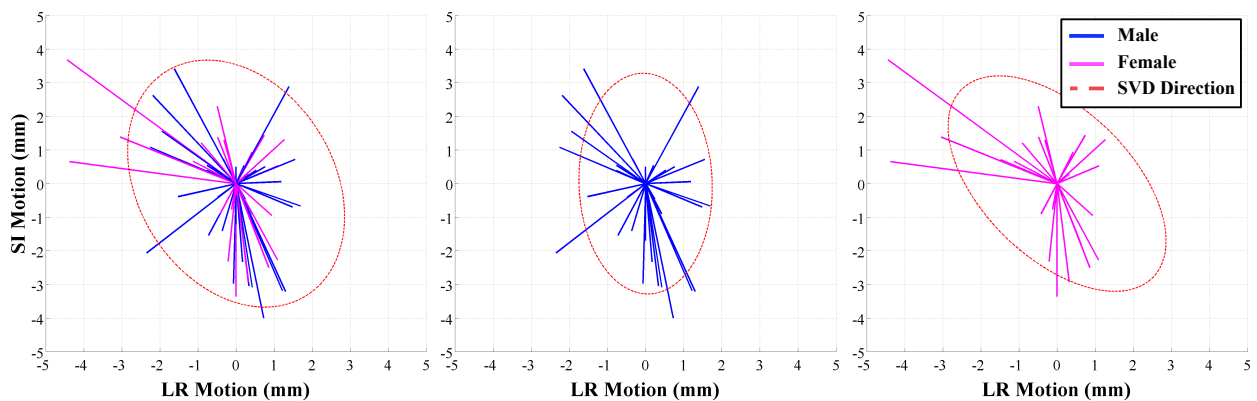
Figure 4-7 Maternal motion for male (blue) and female (magenta) fetuses. The SVD shows that the dominant direction of motion is SI.

The placental location (anterior and posterior) in relation to maternal motion is shown in figure 4-8. There was no significant difference between the anterior and posterior placenta positions in the SI motion (p = 0.67, see table 4-3). There was a statistically significant difference between the anterior and posterior placentas in the LR motion (p = 0.02), and between the LR and SI motion for anteriorly (p = 0.04) and posteriorly (p = 0.0002) located placentas.
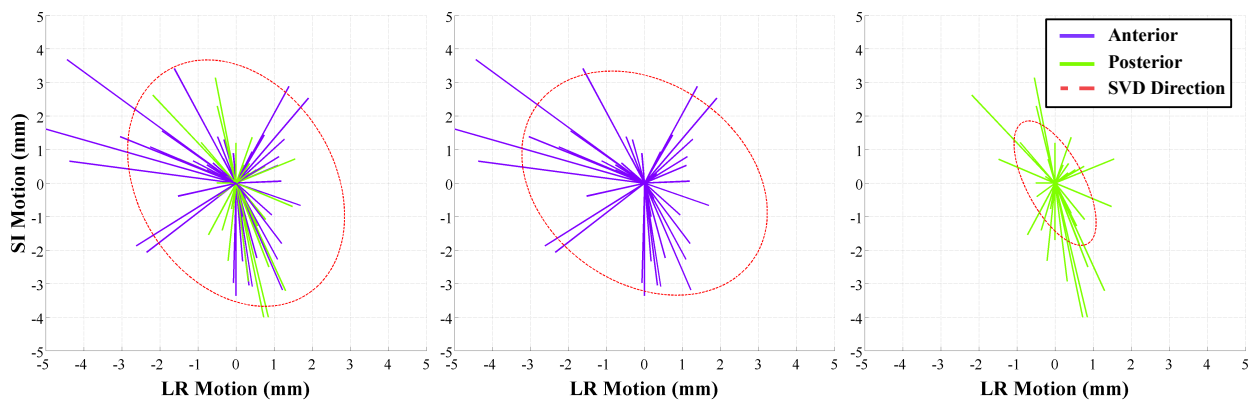
Figure 4-8 Maternal motion for anterior (magenta) and posterior (green) placental locations. The SVD shows that the dominant direction of motion is SI.

No Contraction Cases		SI (mm)	p-value	LR (mm)	p-value
Longitudinal	**1st MRI (n = 50)**	1.3 ± 1.0	0.74	0.6 ± 1.0	0.004
	2nd MRI (n = 37)	1.4 ± 1.1		1.1 ± 0.9	
Fetal Sex	**Male (n = 37)**	1.4 ± 1.2	0.908	0.8 ± 0.7	0.539
	Female (n = 27)	1.4 ± 1.0		0.9 ± 1.2	
Placental Position	**Anterior (n = 49)**	1.4 ± 1.0	0.672	1.1 ± 1.2	0.0245
	Posterior (n = 38)	1.3 ± 1.1		0.6 ± 0.5	
All Cases		1.4 ± 1.0		0.8 ± 1.0	

Table 4-3 Mean motion of SI and LR directions for maternal motion

4.4 Discussion

We used the image-based template-matching algorithm to characterize uterine contraction and maternal motion. SI motion compensation should be corrected for placental MRI scans, especially if the placenta is located in the superior region. The duration of contractions was statistically significant and greater by a mean of 26 seconds during GA 14-18 weeks compared to GA 19-24 weeks. We also observed that there was no association in the direction of motion between fetal sex, placental location, and gestational age. This method can potentially improve uterine motion detection with MRI studies in pregnant patients, thereby avoiding potential motion artifacts.

Dickinson et al. [10] performed a study on uterine contractions, where they monitored the duration of contractions in pregnant women at gestational ages between 20-40 weeks using ambulatory tocodynamometry. In their study they observed that the duration of contractions decreased between 20-24 weeks and 25-28 weeks gestational ages and subsequently began to increase again. Our present study demonstrated a similar decrease in the duration of contractions between the 1st MRI (14-18 weeks gestation age) and the 2nd MRI (19-24 weeks) timing, despite being at earlier gestational ages. Dickinson et al. also showed that the max amplitude of the contractions increased across gestational age. We observed a similar non-significant trend, related to a small sample size.

We also observed that there was no significant difference in the duration and the direction of motion, except in LR motion, for exams included just the maternal motion. Even though there

was a significant difference in LR motion between the 1st and 2nd MRI, the mean maximum motion was 1.1 mm and 0.6 mm, respectively. However, when using multi-resolution in the tracking algorithm with four-fold resolution we encountered a measurement error of ±0.4 mm. Therefore the difference between 1.1 mm and 0.6 mm is considered too small to warrant correction of motion in most applications. Having no significant difference in maternal motion between varying gestational ages, fetal sex, and placental location, it supports the expected notion that uterine motion is random.

The 3D multi-echo golden angle radial VIBE sequence that we used can provide more than just motion characterization. A recent study showed that this sequence can be used for free-breathing fat quantification [94]. Though yet to be clearly understood, future work perhaps could decipher if there indeed is placental fat and whether such quantification could prove to be useful. Since we have collected multiple echoes, it is possible to generate R2* maps thereby providing information on placental oxygenation. Using the motion information, we can reduce motion artifacts in the interpretation of exams that demonstrate significant motion.

One of the limits of our study is the limited number of uterine contractions noted in exams. Even though the mean direction of motion of uterine contractions between the 1st and 2nd MRI was different, there was no statistically significant difference between gestational ages. This lack of statistical difference between gestational ages could be due to an inadequate sample size. However, we observed significant differences in the duration of the contractions between the 1st and 2nd MRI and in relation to the fetal sexes.

Another challenge is the lack of contrast between the placenta, fetus, and other features that the gradient echo sequence provides. This could make it challenging to distinguish causes of uterine motion caused by fetal motion, maternal digestive track, and uterine contractions. As mentioned in the methods an experienced abdominal radiologist and an experienced maternal fetal medicine specialist, to eliminate possible ambiguity of causes of the uterine motion, confirmed the uterine contractions. To further improve the motion tracking other sequences could be used to achieve T2-weighted or T2/T1-weighted image contrast (e.g. spin echo or balanced steady-state free precession), which would provide better contrast images for the motion tracking. However, the trade off is slower image acquisition, banding artifacts, and/or decreased number of slices.

In conclusion, we have demonstrated uterine contractions and maternal motion characterized by an image-based template-matching algorithm. We showed that there is an increase in contraction frequency between 14-18 weeks and 19-24 weeks gestational ages. The duration of uterine contractions between the two gestational ages was significantly different, and the uterine contraction duration was greater in male versus female fetuses. There was no significant association of the direction of motion for uterine contractions based on gestational age, fetal sex, and position of the placenta. We also observed that the maternal motion is not associated with gestational age, fetal sex, and position of the placenta early in gestation during the second trimester.

4.5 Conclusion

We have demonstrated uterine contractions and maternal motion characterized by an image-based template-matching algorithm. We showed that there is an increase in contraction frequency between 14-18 weeks and 19-24 weeks gestational ages. The duration of uterine contractions between the two gestational ages was significantly different, and the uterine contraction duration was greater in male versus female fetuses. There was no significant association of the direction of motion for uterine contractions based on gestational age, fetal sex, and position of the placenta. We also observed that the maternal motion is not associated with gestational age, fetal sex, and position of the placenta early in gestation during the second trimester.

5 SUMMARY AND FUTURE STUDIES

In summary, I have developed an MRI pulse sequence and showed that it can generate a fat-only self-gated signal and potentially allow for more robust motion compensation for liver DCE MRI. I have developed a novel application of the KWIC reconstruction to CT perfusion scans that can allow up to 75% dose reduction compared to the standard clinical procedures. Lastly, using both the 3D golden angle radial vibe sequence and the KWIC reconstruction to reconstruct 3D dynamic images of uterus (gestation age $\geq$ 14 weeks), and applied an image-based motion tracking method to characterize uterine motion during early gestation.

The SGS_F is a very promising technique in improving the needed motion compensation for quantitative evaluation of liver DCE-MRI studies. We showed in healthy volunteers with no contrast injection that the SGS_F can reliable give accurate respiratory information. Then in patient liver DCE-MRI studies we showed that the SGS_F is not contaminated with the contrast

uptake signal. A future study would need to be done to verify the separation of the contrast uptake and respiratory motion by comparing the contrast uptake signal in the liver or other tissue. This could also be done qualitatively by using SGS_F to generate motion compensation images and compare to the motion compensated images of SGS_{OP}.

As mentioned in chapter 2 one of the current challenges is to automatically select the coil that provides the best SGS_F. We demonstrated in non-contrast healthy volunteers that a PCA could be used to combine the coils to get a comparable SGS to conventional methods, however when it was implemented in patient studies with contrast injected the PCA did not provide an optimal SGS and therefore the coil with the best SGS_F was selected empirically. The next experiment would to develop an automated coil selection, to make it more useful in clinical practice. A possible method to explore are using coil clustering developed by Zhang et al[49]. They generated a navigator correlation matrix with all the coils and then used eigenvalue decomposition to separate out the dominant respiratory signals. Another possibility is to use PCA across the z+coil dimension instead of just using it to combine the coils[30,50,95].

Another study would be to develop and apply motion compensation techniques on the 3D dynamic reconstructed images. 3D dynamic images could be reconstructed using total variation compressed sensing to achieve high spatial and temporal resolution[50]. Soft gating could be used to generate pre-contrast, arterial, and venous phases, but there are not enough dynamic images to estimate quantitative perfusion parameters[96]. Non-rigid deformable registration is another possible study that could be performed to reduce motion related artifacts[97].

Using projection undersampling method to reduce radiation dose for CT perfusion imaging has not been well studied. Most current techniques to reduce radiation dose modulate the tube-current or kVp. Undersampling the projections per gantry rotation will have similar challenges to MRI radial trajectory undersampling; therefore similar methods could potentially be used to compensate for undersampling artifacts. Compressed sensing is a promising future direction of this project as it could theoretically be applied to not only dynamic CT imaging, but also static imaging. A next project would be to evaluate compressed sensing methods on static images and compare them to current iterative reconstruction and FBP reconstructions with a similar dose reduction.

The projection undersampling and KWIC reconstruction has great potential to provide another possible pathway to reduce the radiation dose of clinical abdominal perfusion with CT. Due to the high ionizing radiation exposure during continuous CT scanning, CT perfusion in the abdomen is limited. Another project would then to be apply CT KWIC in abdominal cases and compare the KWIC reconstruction with the current standard of practice, which is to scan every 2-3 seconds (even though 1 second temporal resolution is desired).

Another future study using the uterine motion characterization is to apply motion compensation for free-breathing fat quantification[94] and R2* mapping. The fat quantification can help understand the physiological features of the placenta and to assess if there is a difference between healthy and abnormal placenta features. The motion characterization can be

used to remove motion corrupted data to improve the quantification of the placental fat. A recent study assessed the oxygenation in the placenta using R2* mapping based off of the multi-echo sequence[98]. However, some of the subjects, with uterine contractions provided severe motion artifacts that affected the R2* quantification. The motion characterization of the uterine motion can then be used to identify the motion corrupted date and then the data could be removed to decrease the motion bias of the placenta.

Having a fat-only SGS, low dose CT perfusion, and uterine motion characterization are essentials steps to improving quantitative abdominal imaging. Motion corruption is still one of the limiting factors in quantitative MR imaging, and high radiation dose limits the abdominal imaging for CT perfusion. Using these developed techniques can potentially improve and increase the clinical application for quantitative abdominal imaging.

6 REFERENCES

1. Maxwell Parkin D, Bray F, Ferlay J, Pisani P. Estimating the world cancer burden: Globocan 2000. *Int J Cancer*. 2001;94(2):153-156. doi:10.1002/ijc.1440.

2. Befeler AS, di Bisceglie AM. Hepatocellular carcinoma: Diagnosis and treatment. *Gastroenterology*. 2002;122(6):1609-1619. doi:10.1053/gast.2002.33411.

3. Ananth C V. Ischemic placental disease: a unifying concept for preeclampsia, intrauterine growth restriction, and placental abruption. *Semin Perinatol*. 2014;38(3):131-132. doi:10.1053/j.semperi.2014.03.001.

4. Vintzileos AM, Ananth C V. First trimester prediction of ischemic placental disease. *Semin Perinatol*. 2014;38(3):159-166. doi:10.1053/j.semperi.2014.03.006.

5. Ananth C V., Vintzileos AM. Maternal-fetal conditions necessitating a medical intervention resulting in preterm birth. *Am J Obstet Gynecol*. 2006;195(6):1557-1563. doi:10.1016/j.ajog.2006.05.021.

6. Parker SE, Werler MM. Epidemiology of ischemic placental disease: a focus on preterm

gestations. *Semin Perinatol*. 2014;38(3):133-138. doi:10.1053/j.semperi.2014.03.004.

7.   Brau ACS, Brittain JH. Generalized self-navigated motion detection technique: Preliminary investigation in abdominal imaging. *Magn Reson Med*. 2006;55(2):263-270. doi:10.1002/mrm.20785.

8.   Coakley F V., Glenn OA, Qayyum A, Barkovich AJ, Goldstein R, Filly RA. Fetal MRI: A Developing Technique for the Developing Patient. *Am J Roentgenol*. 2004;182(1):243-252. doi:10.2214/ajr.182.1.1820243.

9.   Prayer D, Brugger PC, Prayer L. Fetal MRI: Techniques and protocols. *Pediatr Radiol*. 2004;34(9):685-693. doi:10.1007/s00247-004-1246-0.

10.   Dickinson JE, Godfrey M, Evans SF. Antenatal Patterns of Uterine Activity in Low-Risk Women: A Longitudinal Study. *Aust New Zeal J Obstet Gynaecol*. 1997;37(2):149-152. doi:10.1111/j.1479-828X.1997.tb02242.x.

11.   Hee KS, Dougherty L. Dynamic MRI with projection reconstruction and KWIC processing for simultaneous high spatial and temporal resolution. *Magn Reson Med*. 2004;52(4):815-824. doi:10.1002/mrm.20237.

12.   Song HK, Dougherty L. k-Space weighted image contrast (KWIC) for contrast manipulation in projection reconstruction MRI. *Magn Reson Med*. 2000;44(6):825-832. doi:10.1002/1522-2594(200012)44:6.

13.   Liu P-F, Krestin GP, Huch RA, Göhde SC, Caduff RF, Debatin JF. MRI of the uterus, uterine cervix, and vagina: diagnostic performance of dynamic contrast-enhanced fast multiplanar gradient-echo imaging in comparison with fast spin-echo T2-weighted pulse imaging. *Eur Radiol*. 1998;8(8):1433-1440. doi:10.1007/s003300050569.

14. Ocak I, Bernardo M, Metzger G, et al. Dynamic Contrast-Enhanced MRI of Prostate Cancer at 3 T: A Study of Pharmacokinetic Parameters. *Am J Roentgenol*. 2007;189(4):W192-W201. doi:10.2214/AJR.06.1329.

15. Jager GJ, Ruijter ET, van de Kaa CA, et al. Dynamic TurboFLASH subtraction technique for contrast-enhanced MR imaging of the prostate: correlation with histopathologic results. *Radiology*. 1997;203(3):645-652. doi:10.1148/radiology.203.3.9169683.

16. Wedam SB, Low JA, Yang SX, et al. Antiangiogenic and antitumor effects of bevacizumab in patients with inflammatory and locally advanced breast cancer. *J Clin Oncol*. 2006;24(5):769-777. doi:10.1200/JCO.2005.03.4645.

17. Mayr NA, Yuh WTC, Arnholt JC, et al. Pixel analysis of MR perfusion imaging in predicting radiation therapy outcome in cervical cancer. *J Magn Reson Imaging*. 2000;12(6):1027-1033. doi:10.1002/1522-2586(200012)12:6.

18. Reddick WE, Taylor JS, Fletcher BD. Dynamic MR imaging (DEMRI) of microcirculation in bone sarcoma. *J Magn Reson Imaging*. 1999;10(3):277-285. doi:10.1002/(SICI)1522-2586(199909)10:3.

19. Barentsz JO, Berger-Hartog O, Witjes JA, et al. Evaluation of chemotherapy in advanced urinary bladder cancer with fast dynamic contrast-enhanced MR imaging. *Radiology*. 1998;207(3):791-797. doi:10.1148/radiology.207.3.9609906.

20. Türkbey B, Thomasson D, Pang Y. The role of dynamic contrast-enhanced MRI in cancer diagnosis and treatment. *Diagnostic and*. 2010.

21. Alıcıoglu B, Guler O, Bulakbası N, Akpınar S, Tosun O, Comunoglu C. Utility of semiquantitative parameters to differentiate benign and malignant focal hepatic lesions.

Clin Imaging. 2013;37(4):692-696. doi:10.1016/j.clinimag.2013.01.012.

22. Koh TS, Thng CH, Lee PS, et al. Hepatic Metastases: In Vivo Assessment of Perfusion Parameters at Dynamic Contrast-enhanced MR Imaging with Dual-Input Two-Compartment Tracer Kinetics Model. *Radiology*. 2008;249(1):307-320. doi:10.1148/radiol.2483071958.

23. Materne R, Smith AM, Peeters F, et al. Assessment of hepatic perfusion parameters with dynamic MRI. *Magn Reson Med*. 2002;47(1):135-142. doi:10.1002/mrm.10045.

24. Scharf J, Zapletal C, Hess T, et al. Assessment of hepatic perfusion in pigs by pharmacokinetic analysis of dynamic MR images. *J Magn Reson Imaging*. 1999;9(4):568-572. doi:10.1002/(SICI)1522-2586(199904)9:4.

25. Taouli B, Johnson RS, Hajdu CH, et al. Hepatocellular Carcinoma: Perfusion Quantification With Dynamic Contrast-Enhanced MRI. *Am J Roentgenol*. 2013;201(4):795-800. doi:10.2214/AJR.12.9798.

26. Langen K., Jones DT. Organ motion and its management. *Int J Radiat Oncol*. 2001;50(1):265-278. doi:10.1016/S0360-3016(01)01453-5.

27. Lin W, Guo J, Rosen MA, Song HK. Respiratory motion-compensated radial dynamic contrast-enhanced (DCE)-MRI of chest and abdominal lesions. *Magn Reson Med*. 2008;60(5):1135-1146. doi:10.1002/mrm.21740.

28. Rasche V, Boer RW De, Holz D, Proksa R. Continuous radial data acquisition for dynamic MRI. *Magn Reson Med*. 1995;34(5):754-761. doi:10.1002/mrm.1910340515.

29. Feng L, Grimm R, Block KT obias, et al. Golden-angle radial sparse parallel MRI: combination of compressed sensing, parallel imaging, and golden-angle radial sampling

for fast and flexible dynamic volumetric MRI. *Magn Reson Med*. 2014;72(3):707-717. doi:10.1002/mrm.24980.

30.   Feng L, Axel L, Chandarana H, Block KT, Sodickson DK, Otazo R. XD-GRASP: Golden-angle radial MRI with reconstruction of extra motion-state dimensions using compressed sensing. *Magn Reson Med*. 2016;00(2):n/a-n/a. doi:10.1002/mrm.25665.

31.   Winkelmann S, Schaeffter T, Koehler T, Eggers H, Doessel O. An optimal radial profile order based on the golden ratio for time-resolved MRI. *IEEE Trans Med Imaging*. 2007;26(1):68-76. doi:10.1109/TMI.2006.885337.

32.   Larson AC, White RD, Laub G, McVeigh ER, Li D, Simonetti OP. Self-gated cardiac cine MRI. *Magn Reson Med*. 2004;51(1):93-102. doi:10.1002/mrm.10664.

33.   Spincemaille P, Liu J, Nguyen T, Prince MR, Wang Y. Z intensity-weighted position self-respiratory gating method for free-breathing 3D cardiac CINE imaging. *Magn Reson Imaging*. 2011;29(6):861-868. doi:10.1016/j.mri.2011.02.011.

34.   Larson AC, Kellman P, Arai A, et al. Preliminary investigation of respiratory self-gating for free-breathing segmented cine MRI. *Magn Reson Med*. 2005;53(1):159-168. doi:10.1002/mrm.20331.

35.   Martin T, Saucedo A, Armstrong T, Wu H, Wang DJ, Sung K. 3D Stack-of-Stars Dixon Fat-Only Signal for Respiratory Motion Detection. In: *Proceedings 24th Scientific Meeting, International Society for Magnetic Resonance in Medicine*. ; 2016:4262.

36.   Martin T, Armstrong T, Felker E, et al. Respiratory Motion Compensation in the Liver using Fat-Only Self Gated Signal. In: *Proceedings 25th Scientific Meeting, International Society for Magnetic Resonance in Medicine*. ; 2017:1026.

37. Dixon W. Simple proton spectroscopic imaging. *Radiology*. 1984.

38. Guiu B, Petit J-M, Loffroy R, et al. Quantification of Liver Fat Content: Comparison of Triple-Echo Chemical Shift Gradient-Echo Imaging and in Vivo Proton MR Spectroscopy. *Radiology*. 2009;250(1):95-102. doi:10.1148/radiol.2493080217.

39. Hernando D, Vigen KK, Shimakawa A, Reeder SB. R?2* mapping in the presence of macroscopic B0 field variations. *Magn Reson Med*. 2012;68(3):830-840. doi:10.1002/mrm.23306.

40. Hernando D, Kramer JH, Reeder SB. Multipeak fat-corrected complex R2* relaxometry: Theory, optimization, and clinical validation. *Magn Reson Med*. 2013;70(5):1319-1331. doi:10.1002/mrm.24593.

41. Golub~ GH, Reinsch C. Handbook Series Linear Algebra Singular Value Decomposition and Least Squares Solutions*. 14:403-420.

42. Bashir MR, Castelli P, Davenport MS, et al. Respiratory Motion Artifact Affecting Hepatic Arterial Phase MR Imaging with Gadoxetate Disodium Is More Common in Patients with a Prior Episode of Arterial Phase Motion Associated with Gadoxetate Disodium. *Radiology*. 2015;274(1):141-148. doi:10.1148/radiol.14140386.

43. Benkert T, Block KT, Heller S, et al. Comprehensive Dynamic Contrast-Enhanced 3D Magnetic Resonance Imaging of the Breast With Fat/Water Separation and High Spatiotemporal Resolution Using Radial Sampling, Compressed Sensing, and Parallel Imaging. *Invest Radiol*. 2017;52(10):583-589. doi:10.1097/RLI.0000000000000375.

44. Skinner TE, Glover GH. An extended two-point dixon algorithm for calculating separate water, fat, andB0 images. *Magn Reson Med*. 1997;37(4):628-630.

doi:10.1002/mrm.1910370426.

45.   Ma J. Breath-hold water and fat imaging using a dual-echo two-point dixon technique with an efficient and robust phase-correction algorithm. *Magn Reson Med*. 2004;52(2):415-419. doi:10.1002/mrm.20146.

46.   Glover G, Schneider E. Three‑point dixon technique for true water/fat decomposition with B0 inhomogeneity correction. *Magn Reson Med*. 1991.

47.   Brodsky EK, Holmes JH, Yu H, Reeder SB. Generalizedk-space decomposition with chemical shift correction for non-cartesian water-fat imaging. *Magn Reson Med*. 2008;59(5):1151-1164. doi:10.1002/mrm.21580.

48.   Armstrong T, Dregely I, Stemmer A, et al. Free-breathing liver fat quantification using a multiecho 3D stack-of-radial technique. *Magn Reson Med*. April 2017. doi:10.1002/mrm.26693.

49.   Zhang T, Cheng JY, Chen Y, Nishimura DG, Pauly JM, Vasanawala SS. Robust self-navigated body MRI using dense coil arrays. *Magn Reson Med*. 2016;76(1):197-205. doi:10.1002/mrm.25858.

50.   Fujimoto K, Feng L, Otazo R, et al. GRASP with Motion Compensation for DCE-MRI of the Abdomen. In: *Proceedings 25th Scientific Meeting, International Society for Magnetic Resonance in Medicine*. ; 2017.

51.   Donahue J, Wintermark M. Perfusion CT and acute stroke imaging: Foundations, applications, and literature review. *J Neuroradiol*. 2015;42(1):21-29. doi:10.1016/j.neurad.2014.11.003.

52.   Wintermark M, Albers GW, Alexandrov A V, et al. Acute stroke imaging research

roadmap. *AJNR Am J Neuroradiol*. 2008;29(5):e23-30. doi:10.1161/STROKEAHA.107.512319.

53.   Wintermark M, Lev M. FDA investigates the safety of brain perfusion CT. *Am J*. 2010.

54.   Othman AE, Afat S, Brockmann MA, et al. Radiation dose reduction in perfusion CT imaging of the brain: A review of the literature. *J Neuroradiol*. 2016;43(1):1-5. doi:10.1016/j.neurad.2015.06.003.

55.   Lee TY, Chhem RK. Impact of new technologies on dose reduction in CT. *Eur J Radiol*. 2010;76(1):28-35. doi:10.1016/j.ejrad.2010.06.036 [doi].

56.   2016 AAPM - Adult Brain Perfusion CT Protocols. American Association of Physicists in Medicine   website. http://www.aapm.org/pubs/CTProtocols/documents/AdultBrainPerfusionCT.pdf. Published 2016.

57.   ROUTINE   CT   HEAD   (BRAIN). http://www.aapm.org/pubs/CTProtocols/documents/AdultRoutineHeadCT.pdf.   Published 2016. Accessed March 17, 2017.

58.   Geyer LL, Schoepf UJ, Meinel FG, et al. State of the Art: Iterative CT Reconstruction Techniques. *Radiology*. 2015;276(2):339-357. doi:10.1148/radiol.2015132766.

59.   Noël P, Fingerle A, Renger B. A clinical comparison study of a novel statistical iterative and filtered backprojection reconstruction. *Proc*. 2011.

60.   Funama Y, Taguchi K, Utsunomiya D, et al. Combination of a low-tube-voltage technique with hybrid iterative reconstruction (iDose) algorithm at coronary computed tomographic angiography. *J Comput Assist Tomogr*. 2011;35(4):480-485.

doi:10.1097/RCT.0b013e31821fee94.

61.   Niesten JM, Schaaf IC, Riordan AJ, et al. Radiation dose reduction in cerebral CT perfusion imaging using iterative reconstruction. *Eur Radiol*. 2014;24(2):484-493.

62.   Mistretta CA. Undersampled radial MR acquisition and highly constrained back projection (HYPR) reconstruction: Potential medical imaging applications in the post-Nyquist era. *J Magn Reson Imaging*. 2009;29(3):501-516. doi:10.1002/jmri.21683.

63.   Krissak R, Mistretta C, Henzler T. Noise reduction and image quality improvement of low dose and ultra low dose brain perfusion CT by HYPR-LR processing. *PLoS*. 2011.

64.   Supanich M, Tao Y, Nett B, Pulfer K. Radiation dose reduction in time-resolved CT angiography using highly constrained back projection reconstruction. *Phys Med*. 2009.

65.   Martin T, Hoffman J, Alger JR, McNitt-Gray M, Wang DJ. Low-dose CT perfusion with projection view sharing. *Med Phys*. 2018;45(1):101-113. doi:10.1002/mp.12640.

66.   Rasche V, Proksa R, Sinkus R, Bornert P, Eggers H. Resampling of data between arbitrary grids using convolution interpolation. *IEEE Trans Med Imaging*. 1999;18(5):385-392. doi:10.1109/42.774166.

67.   Bushberg JT, Seibert JA, Leidholdt EM, Boone JM. *The Essential Physics of Medical Imaging*.; 2011.

68.   Stierstorfer K, Rauscher A, Boese J, Bruder H, Schaller S, Flohr T. Weighted FBP--a simple approximate 3D FBP algorithm for multislice spiral CT with good dose usage for arbitrary pitch. *Phys Med Biol*. 2004;49(11):2209-2218. doi:10.1088/0031-9155/49/11/007.

69.   Flohr TG, Stierstorfer K, Ulzheimer S, Bruder H, Primak a N, McCollough CH. Image

reconstruction and image quality evaluation for a 64-slice CT scanner with z-flying focal spot. *Med Phys*. 2005;32(8):2536-2547. doi:10.1118/1.1949787.

70. Hoffman J, Young S, Noo F, McNitt-Gray M. Technical Note: FreeCT_wFBP: A robust, efficient, open-source implementation of weighted filtered backprojection for helical, fan-beam CT. *Med Phys*. 2016;43(3):1411-1420. doi:10.1118/1.4941953.

71. Wundrak S, Paul J, Ulrici J, et al. Golden ratio sparse MRI using tiny golden angles. *Magn Reson Med*. 2016;75(6):2372-2378. doi:10.1002/mrm.25831.

72. Benner T, Heiland S, Erb G, Forsting M. Accuracy of gamma-variate fits to concentration-time curves from dynamic susceptibility-contrast enhanced MRI: influence of time resolution, maximal signal drop and. *Magn Reson*. 1997.

73. Kidwell CS, Jahan R, Gornbein J, et al. A Trial of Imaging Selection and Endovascular Treatment for Ischemic Stroke. *N Engl J Med*. 2013;368(10):914-923. doi:10.1056/NEJMoa1212793.

74. Wintermark M, Maedar T, Schnyder P, Meuli R. Quantitative assessment of regional cerebral blood flows by perfusion CT studies at low injection rates: a critical review of the underlying theoretical models. *Eur Radiol*. 2001;11:1220-1230.

75. Gamper U, Boesiger P, Kozerke S. Compressed sensing in dynamic MRI. *Magn Reson Med*. 2008;59(2):365-373. doi:10.1002/mrm.21477.

76. Salomon EJ, Barfett J, Willems PWA, Geibprasert S, Bacigaluppi S, Krings T. Dynamic CT Angiography and CT Perfusion Employing a 320-Detector Row CT. *Clin Neuroradiol*. 2009;19(3):187-196. doi:10.1007/s00062-009-9019-7.

77. van Heeswijk RB, Piccini D, Feliciano H, Hullin R, Schwitter J, Stuber M. Self-navigated

isotropic three-dimensional cardiac T$_2$ mapping. *Magn Reson Med*. 2015;73(4):1549-1554. doi:10.1002/mrm.25258.

78. Wundrak S, Paul J, Ulrici J, Hell E, Rasche V. A Small Surrogate for the Golden Angle in Time-Resolved Radial MRI Based on Generalized Fibonacci Sequences. *IEEE Trans Med Imaging*. 2015;34(6):1262-1269. doi:10.1109/TMI.2014.2382572.

79. Wu Y, Wieben O, Mistretta CA, Korosec FR. Evaluation of temporal and spatial characteristics of 2D HYPR processing using simulations. *Magn Reson Med*. 2008;59(5):1090-1098. doi:10.1002/mrm.21564.

80. Keith L, Rahimi M, Holmes J, Brittain J, Korosec F. Use of a computer-controlled motion phantom to investigate the temporal and spatial fidelity of HYPR processing. *Magn Reson Med*. 2014;71(2):702-710. doi:10.1002/mrm.24707.

81. O'Halloran RL, Wen Z, Holmes JH, Fain SB. Iterative projection reconstruction of time-resolved images using highly-constrained back-projection (HYPR). *Magn Reson Med*. 2008;59(1):132-139. doi:10.1002/mrm.21439.

82. Song HK, Yan L, Smith RX, et al. Noncontrast enhanced four-dimensional dynamic MRA with golden angle radial acquisition and k-space weighted image contrast (KWIC) reconstruction. *Magn Reson Med*. 2014;72(6):1541-1551. doi:10.1002/mrm.25057.

83. Hernandez RJ, Goodsitt MM. Reduction of radiation dose in pediatric patients using pulsed fluoroscopy. *AJR Am J Roentgenol*. 1996;167(5):1247-1253. doi:10.2214/ajr.167.5.8911190.

84. Hell E, Mattern D, Schardt P. X-ray tube with flying focus. *US Pat 6,292,538*. 2001.

85. Ketelsen D, Buchgeister M, Fenchel M, et al. Automated Computed Tomography Dose-

Saving Algorithm to Protect Radiosensitive Tissues. *Invest Radiol*. 2012;47(2):148-152. doi:10.1097/RLI.0b013e3182311504.

86. Derwig IE, Akolekar R, Zelaya FO, Gowland PA, Barker GJ, Nicolaides KH. Association of placental volume measured by MRI and birth weight percentile. *J Magn Reson Imaging*. 2011;34(5):1125-1130. doi:10.1002/jmri.22794.

87. Damodaram M, Story L, Eixarch E, et al. Placental MRI in Intrauterine Fetal Growth Restriction. 2010. doi:10.1016/j.placenta.2010.03.001.

88. Thomson AM, Billewicz WZ, Hytten FE. THE WEIGHT OF THE PLACENTA IN RELATION TO BIRTHWEIGHT. *BJOG An Int J Obstet Gynaecol*. 1969;76(10):865-872. doi:10.1111/j.1471-0528.1969.tb15722.x.

89. Angtuaco TL, Shah HR, Mattison DR, Quirk JG. MR imaging in high-risk obstetric patients: a valuable complement to US. *Radiographics*. 1992;12(1):91-109; discussion 110. doi:10.1148/radiographics.12.1.1734485.

90. Shellock FG. Policies, guidelines, and recommendations for MR imaging safety and patient management. *J Magn Reson Imaging*. 1991;1(1):97-101. doi:10.1002/jmri.1880010114.

91. Sletten J, Kiserud T, Kessler J. Effect of uterine contractions on fetal heart rate in pregnancy: a prospective observational study. *Acta Obstet Gynecol Scand*. 2016;95(10):1129-1135. doi:10.1111/aogs.12949.

92. Wu HH, Gurney PT, Hu BS, Nishimura DG, McConnell M V. Free-breathing multiphase whole-heart coronary MR angiography using image-based navigators and three-dimensional cones imaging. *Magn Reson Med*. 2013;69(4):1083-1093.

doi:10.1002/mrm.24346.

93.   Zia S. Placental location and pregnancy outcome. *J Turkish Ger Gynecol Assoc*. 2013;14(4):190-193. doi:10.5152/jtgga.2013.92609.

94.   Armstrong T, Dregely I, Stemmer A, et al. Free-breathing liver fat quantification using a multiecho 3D stack-of-radial technique. *Magn Reson Med*. 2018;79(1):370-382. doi:10.1002/mrm.26693.

95.   Feng L, Huang C, Shanbhogue K, Sodickson DK, Chandarana H, Otazo R. RACER-GRASP: Respiratory-weighted, aortic contrast enhancement-guided and coil-unstreaking golden-angle radial sparse MRI. *Magn Reson Med*. 2018;80(1):77-89. doi:10.1002/mrm.27002.

96.   Han F, Zhou Z, Han E, et al. Self-gated 4D multiphase, steady-state imaging with contrast enhancement (MUSIC) using rotating cartesian K-space (ROCK): Validation in children with congenital heart disease. *Magn Reson Med*. 2017;78(2):472-483. doi:10.1002/mrm.26376.

97.   Cheng JY, Zhang T, Ruangwattanapaisarn N, et al. Free-breathing pediatric MRI with nonrigid motion correction and acceleration. *J Magn Reson Imaging*. 2015;42(2):407-420. doi:10.1002/jmri.24785.

98.   Armstrong T, Liu D, Martin T, et al. 3D R2* Mapping of the Placenta During Early Gestation Using Free-Breathing Multiecho Stack-of-Radial MRI at 3 T. *J Magn Reson Imaging*. 2018. doi:In Press.